Earthquake Science 37 (2024) 277–303

Contents lists available at ScienceDirect

Earthquake Science

Journal homepage: https://www.keaipublishing.com/en/journals/earthquake-science/

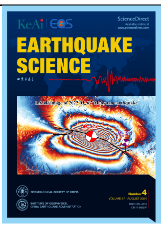

Article

Co and postseismic fault slip models of the 2022 M_W6.7 Menyuan earthquake reveal conjugated faulting tectonics at the central section of the Lenglongling fault

Zilong He[1,2], Wenbin Xu[1,2,✉], Zhiwei Li[1,2], Lei Xie[1,2], Guangcai Feng[1,2], Nan Fang[1,2], Xiaoge Liu[1,2], Kai Sun[1,2], Zhidan Chen[1,2] and Zhihui Zhu[3]

[1] *School of Geosciences and Info-Physics*, *Central South University*, *Changsha* 410083, *China*
[2] *Key Laboratory of Metallogenic Prediction of Nonferrous Metals and Geological Environment Monitoring*, *Central South University*, *Changsha* 410083, *China*
[3] *School of Civil Engineering*, *Central South University*, *Changsha* 410083, *China*

Key points:

- We inverted the rupture process of the Menyuan mainshock using seismic and geodetic data that shows a maximum slip of ~3 m on the Lenglongling fault.
- We found postseismic transient deformation at the Lenglongling fault and afterslip occurred primarily at the depth between 10 km and 15 km.
- A high-angle conjugated faulting event was triggered by the mainshock at the middle section of the Lenglongling fault that probably helped terminate the rupture.

ABSTRACT

The 2022 M_W6.7 Menyuan earthquake ruptured the western end of the Tianzhu seismic gap, providing an opportunity to study the regional seismogenic characteristics and seismic hazards. Here we use interferometric synthetic aperture radar (InSAR) and seismic data to study the mainshock rupture, early afterslip and the second largest aftershock of the 2022 Menyuan earthquake sequences. Our modeling results show that the mainshock ruptured the Lenglongling fault and the Tuolaishan fault with a maximum slip of ~3 m. Rapid postseismic transient deformation occurred at the center of the Lenglongling fault. Our afterslip modeling reveals that the majority of afterslip occurred in the deeper part of the Lenglongling fault. A high-angle conjugated faulting event is found at the middle section of the Lenglongling fault. We use the stress inversion to investigate the possible triggering mechanism of the conjugated rupture event. The results indicate the maximum principal stress direction is in ~222°, forming a ~22° angle between the conjugated fault of second largest aftershock and the mainshock. The calculated normal stress changes indicate the region is within a pull-apart stress field, which favors such a conjugated rupturing event. Our study will help understand the rupture behavior of such kind of conjugated fault in other regions.

Production and Hosting by Elsevier on behalf of KeAi

✉ **Corresponding author.** Xu WB, email: wenbin.xu@csu.edu.cn

Article history:
Received 26 October 2023
Received in revised form 29 December 2023
Accepted 6 January 2024
Available online 28 February 2024

https://doi.org/10.1016/j.eqs.2024.04.008

Keywords: coseismic displacement and slip; postseismic deformation and afterslip; conjugate rupture; coulomb stress change; stress inversion

Citation: He ZL, Xu WB, Li ZW, Xie L, Feng GC, Fang N, Liu XG, Sun K, Chen ZD and Zhu ZH (2024). Co and postseismic fault slip models of the 2022 M_{W}6.7 Menyuan earthquake reveal conjugated faulting tectonics at the central section of the Lenglongling fault. Earthq Sci **37**(4): 277–303, doi: 10.1016/j.eqs.2024.04.008.

1. Introduction

The transfer of tectonic stress from the plate boundaries to the interior of continents causes devastating earthquakes and large-scale tectonic deformation within continents (Yin A and Harrison, 2000; Zhang PZ et al., 2004). The Haiyuan fault, a large-scale strike-slip fault on the northeastern margin of the Qinghai-Xizang Plateau, results from the northward expansion of crustal shortening (Huang ZC et al., 2022; Métivier et al., 1998; Wang WT et al., 2022). Although this fault is more than 1 000 km from the collision boundary between India and Eurasia, it hosted some disastrous seismic events, such as the 1920 ~M8.5 Haiyuan and 1927 ~M8 Gulang earthquakes (Lasserre et al., 1999; Liu-Zeng J et al., 2007). The 1920 event was responsible for a 230 km surface rupture and more than 10-m coseismic displacement with a maximum strike-slip in the eastern section of the Haiyuan fault (Lasserre et al., 1999; Ou Q et al., 2020). The middle section of the Haiyuan fault is referred to as the Tianzhu seismic gap because the paleoseismic studies exhibit notable faulted landforms but no major seismic record during the past 1 000 years in this region (Gaudemer et al., 1995; Liu-Zeng J et al., 2007; Zhang PZ et al., 2005). Thus, this seismic gap draws wide attention due to its intense tectonic activity, adjacent strong seismic records, and potential seismic hazards (Liu HZ et al., 2023).

The M_{W}6.7 Menyuan earthquake, on January 8, 2022, occurred at the western end of the Tianzhu seismic gap and ruptured the Lenglongling fault (LLLF) and the Tuolaishan fault (TLSF) (Liu JH et al., 2022; Yang HF et al., 2022) (Figure 1), causing severe damage to infrastructures (Ji ZW et al., 2022). Its occurrence verifies the high seismic hazards in the middle section of the Haiyuan fault and provides a rare chance to understand the seismogenic characteristics and regional seismic activity. According to field investigations, focal mechanisms, and geodetic observations, the 2022 Menyuan earthquake is found to be a typical left-lateral seismic event (Feng WP et al., 2023; Han S et al., 2022; Liu JH et al., 2022), with only 50 km of surface rupture in the western segment of the Tianzhu seismic gap, suggesting that there is still a roughly 200 km of the seismic region with the possibility of a catastrophic earthquake (Cavalié et al., 2008; Han LF et al., 2021; Huang ZC et al., 2022; Liu JH et al., 2022; Shao YX et al., 2021; Zheng WJ et al., 2013). The limited surface rupture of the Menyuan earthquake provides the opportunity to study the controlling factors of such strike-slip earthquakes, which is crucial for evaluating future seismic hazards in the northeastern Qinghai-Xizang Plateau.

Both static and kinematic slip models of the 2022 Menyuan earthquake have been studied using optical, InSAR, teleseismic and high-rate GNSS data (Bao X et al., 2022; Feng WP et al., 2023; He LJ et al., 2024; Li YS et al., 2022; Lü MZ et al., 2022; Luo H and Wang T, 2022). Although the coseismic slip models of the 2022 Menyuan earthquake have been well studied, there are few postseismic transient deformation fields and afterslip models of this event. Additionally, according to the study of the focal mechanisms by Fan LP et al. (2022) and Feng WP et al. (2023), the second largest aftershocks (M_{W}= 5.12) struck the Menyuan area following the mainshock, occurring at the center of LLLF. The uncertainty of the fault plane solution makes it difficult to distinguish the focal mechanism of this aftershock, and to determine whether it happened on a nearly conjugate fault or not. While Han S et al. (2022) observed ~3 m strike-slip deformation near the LLLF and ~0.8 m horizontal and ~1.5 m vertical deformation caused by a dextral-normal fault at the middle-eastern part of LLLF, which may indicate the possible high-angle rupture. The modeling of the postseismic deformation is thus crucial for us to understand the possible interaction mechanisms of the mainshock, afterslip and the second largest aftershock, and for further evaluating the seismic risk of this region.

In this study, we utilize the seismic and geodetic data to study the coseismic and postseismic slip, as well as the slip model of the second largest aftershock. We use the teleseismic and InSAR data to jointly invert the rupture process of the 2022 Menyuan mainshock. We then acquire the postseismic transient deformation ~2 months following the mainshock by applying a cluster-based empirical correction method. We test the robustness of the derived afterslip models through the Monte-carol simulation and resolution test. We study the relationship between the Coulomb stress change and aftershocks distribution, and analyzed the possible reason for conjugated faulting using

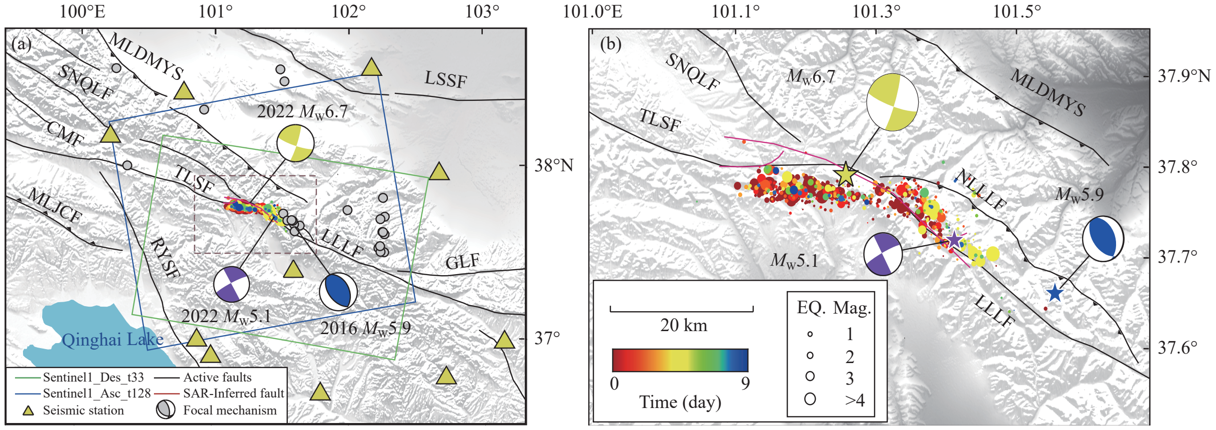

Figure 1. The regional tectonic map of the 2022 Menyuan earthquake. This earthquake ruptured both the Tuolaishan fault and the Lenglongling fault, both of which are strike-slip faults. The 2016 Menyuan earthquake occurred very close to this area, here shown with (a). The dark black line represents the major faults in this area. LSSF: Longshoushan fault; GLF: Gulang fault; LLLF: Lenglongling fault; TLSF: Tuolaishan fault; RYSF: Riyueshan fault; MLDMY: Minle-Damaying fault; SNQLF: Sunan-Qilian fault; CMF: Changma fault; MLJCF: Muli-Jiangcuo fault; NLLF: North Lenglongling fault. The yellow beach ball represents the mechanism of the 2022 Menyuan earthquake in this study and the blue beach ball represents the mechanism of the 2016 Menyuan earthquake (Wang H et al., 2017). The purple beach ball represents the mechanism of the second largest aftershock. The yellow triangles denote the seismic stations utilized in this study. The colored dots represent the relocated aftershocks (Fan LP et al., 2022). The rectangles represent the coverage of different SAR data. The study area is denoted by the gray dashed rectangle. The gray dots denote the historic earthquake mechanisms ($M_W \geq 3.25$) used for stress inversion. (b) The enlarged image of the study area in (a), with the pink line representing the SAR-inferred ruptured faults. The yellow, blue, and purple stars represent the epicenters of the 2022 Menyuan mainshock, 2016 Menyuan mainshock and the second largest aftershock of the 2022 Menyuan earthquake, respectively. The circles denote the relocated aftershocks colored by time, with the size representing the magnitudes.

the regional stress field and normal stress changes on the conjugated fault induced by the coseismic and postseismic slip. Finally, the regional seismic hazards are analyzed using the coseismic, postseismic, and second largest aftershock slip models.

2. Data and methods

2.1. Coseismic InSAR and teleseismic data processing

We used both teleseismic and InSAR data to jointly retrieve the dynamic rupture process of the 2022 Menyuan earthquake. We picked 15 vertical components of P waveforms and 21 longitudinal components of SH waveforms at the epicentral distance between 30°–90° from the Data Management Center of the Incorporated Research Institutions for Seismology. After removing the instrumental response of these records, we integrated them into displacement and applied a band-pass filter between 0.01–0.9 Hz and resampled the waveforms to 5 Hz. We utilized Sentinel-1 images (Table S1 in the Supplementary), spanning 3 days before the earthquake to 38 days after the earthquake, to derive the coseismic and early postseismic deformation of the Menyuan earthquake. The GAMMA software was utilized to process the data by implementing the Differential InSAR (D-InSAR) method. Owning to the high coregistration requirements for the terrain observation by progressive scan imaging (TOPS) mode data, the spectral diversity method (Scheiber and Moreira, 2000) was applied to the data after the finish of the initial coarse coregistration. Then a 20×4 multi-looking process was performed and a 30 m Shuttle Radar Topography Mission digital elevation model was introduced to remove the topographic phase. To further reduce the noise, we applied the Goldstein filter (Goldstein and Werner, 1998) to the interferograms, followed by the phase unwrapping process using the minimum cost flow algorithm (Chen CW and Zebker, 2001).

We masked the near-field data of the coseismic interferogram due to decorrelation and unwrapping error caused by significant deformation gradient. To complement the constraint of near-field InSAR measurement to inversion, we implemented the offset-tracking algorithm (Michel et al., 1999) to derive the range offsets from both the ascending and descending SAR images. To reduce the noise, we set the oversampling factor of 2 and window size of 200 × 100 pixels (range × azimuth) respectively.

2.2. Postseismic InSAR data with clustering based empirical correction method

Considering the postseismic deformation was severely contaminated by the atmospheric delay signal, we sought to mitigate its influence and retrieve the accurate deformation field before modeling the afterslip and second largest aftershock. Several established methods were applied in this study (e.g., Generic Atmospheric Correction Online Service (GACOS) (Yu C et al., 2017), linear correction function (Elliott et al., 2008)), while these methods were proved to be effective in many other cases, they failed to capture the spatially varying height-correlated atmospheric delay in the postseismic interferograms (Figures 2, 3, S1, and S2). This can be attributed to the poor space-time resolution of the external weather model and the breaks down of consistent tropospheric characteristics over the whole image (Wu XX et al., 2023).

To overcome these limitations, we combined the cluster-based image segmentation method with the empirical function correction to mitigate these height-correlated tropospheric delay signals. The *K*-means clustering method

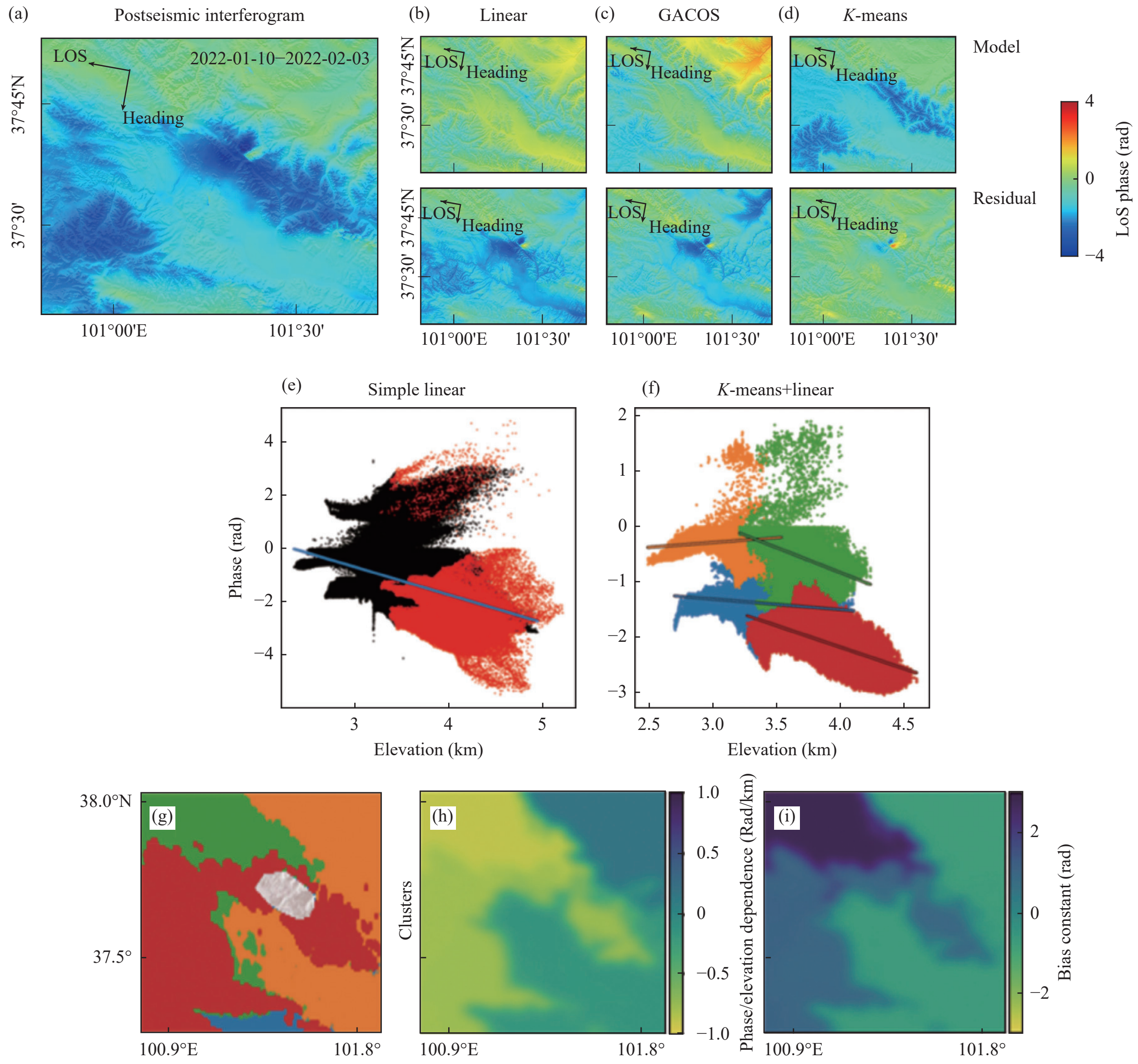

Figure 2. Example showing atmospheric delay correction results using the linear, GACOS, and cluster-based empirical function correction methods. (a) Line of sight (LOS) displacement from descending track of postseismic interferogram spanning from January 10, 2022 to February 3, 2022. (b–d) Atmospheric delay and corrected residuals derived by the linear, the GACOS and the cluster-based empirical function method. (e) Simple linear model to estimate the atmospheric delay. The black points correspond to the raw interferometric phase, whereas the red points denote the interferometric phase after masking out the deformation area. (f) Simple linear model with the cluster method to estimate the atmospheric delay. Different colors represent different clusters. (g) Clustering results of the postseismic interferogram. (h) The slopes between the phase and elevation. (i) The constant coefficient of the linear model.

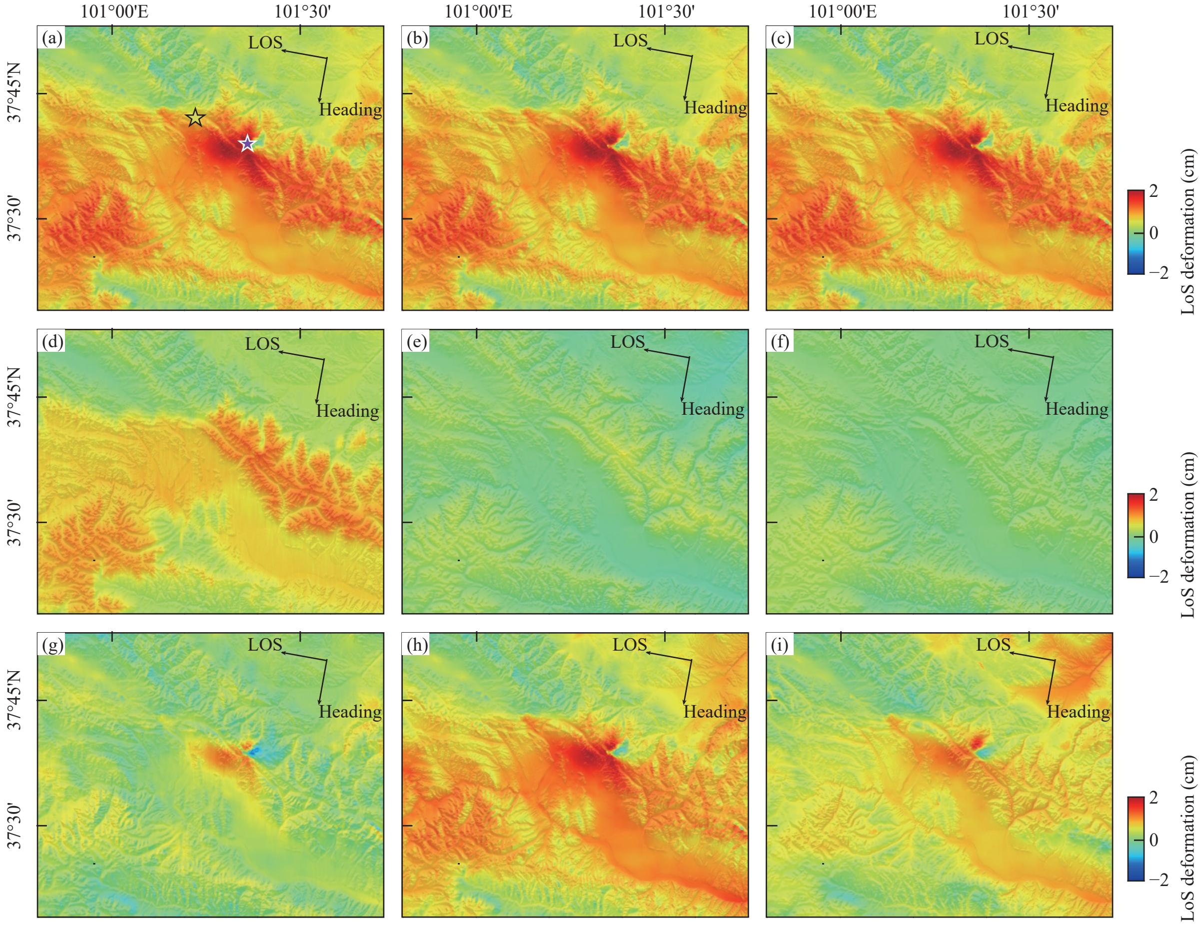

Figure 3. Postseismic LOS displacement from descending track, atmospheric delay correction maps, and the corrected interferograms. (a–c) represent LOS displacement from raw postseismic interferograms spanning 2 days to 38 days after mainshock. (d–f) represent the atmospheric delay corrections derived by the cluster-based empirical method, the linear function method, and the GACOS, respectively. (g–i) are the interferograms after correction.

was adopted here to automatically segment the image with the input of interferogram phase, latitude, longitude and elevation and to determine the cluster centroids and the nearest data belonging to them through iteration (Murray et al., 2021) (Figures 3, S3 and S4). The equations of the cluster generation process can be expressed as:

$$C_k = \{X_j \,|\, \mathrm{argmin}_k (X_j, \mu_k)\}, \tag{1}$$

$$\mu_k = \frac{1}{|C_k|} \sum_{X_j \in C_k} X_j, \tag{2}$$

where, $1 \le j \le$ ndc and $1 \le k \le$ ncc, where ndc and ncc represent the number of input data points and the number of generated clusters, respectively. The X represents the input data set for cluster generation, where each row corresponds to an InSAR data point, and each column represents the features, including latitude, longitude, elevation and interferograms phase. C is the set of data points assigned to each cluster and μ represents the cluster centroids based on the mean of the data points assigned to the cluster. The optimal cluster number was determined through the trade-off curve of the total root mean square (RMS) of the data and the cluster number. Four clusters were found to be adequate for improving the results (Figure S5 in the Supplementary). We masked out the data near the LLLF and TLSF to prevent the possible removal of the postseismic deformation signal. We whitened the data beforehand to remove redundant information from the data. The farthest 5% of data points to each cluster centroid were removed using a support vector machine (SVM) method. The height-correlated atmospheric delay was estimated through the linear function (Figure 2f). After deriving the function parameters, a Gaussian filter of 7 km × 7 km window size was applied to reduce the sharp changes between different clusters. With the spatially varying slope and constant maps (Figure 2h and i), we could derive the height-correlated tropospheric delay using the Digital Elevation Model (DEM) (Farr et al., 2007). To evaluate the efficacy of the correction method, we calculated the semivariogram of the residual after correction from the far-field area (Figure S5b in the Supplementary). The overall semivariance drops by ~60%, with the average decreasing from ~0.36 cm to ~0.14 cm. The remaining signal, especially those with spatial scales less than 20 km, could be attributed to atmospheric turbulence. The uniform correction method and GACOS show poor efficacy in this case (Figures 2, 3, S1, S2, and S5).

2.3. Slip inversion method

2.3.1 Coseismic rupture inversion

To improve the efficiency of the inversion process, we downsampled the coseismic deformation field using a gradient-based quadtree sampling method (Gao H et al., 2021; Simons et al., 2002) (Figure S6 in the Supplementary), and both the InSAR and range offset field were used in the inversion of slip model (Table S2 in the Supplementary). We adopted a two-step inversion strategy to determine the model parameters (Xu WB, 2017). Firstly, we implemented the nonlinear inversion to determine the fault geometry and uniform slip under the assumption of homogeneous elastic space (Okada, 1985). This process was carried out by utilizing the inversion method based on Bayesian theory and Monte Carlo sampling (Vasyura-Bathke et al., 2020), and a one-segment fault was adapted to fit the deformation field. During the inversion, the strike and location of the fault were initially set according to the range offset field (Figure 4) and the dip of fault was bounded within 23° of the prior value provided by the focal mechanism of the United State Geological Survey (USGS) (Table S3 in the Supplementary). After finding the optimal dip, we refined the location of the fault and constructed a strike-variable fault geometry according to the surface fault trace acquired from offset tracking results, and the fault was further enlarged and discretized into 2 km×2 km sub-patches. A multi-time-window method was then employed to invert the kinematic rupture process of the mainshock. The coseismic kinematic inversion method builds on the representation theorem (Aki and Richards, 2002) and regards the sub-patches as point sources. To stabilize the inversion result, the Laplacian smoothing operation was applied to the model parameters, and the final inversion equation can be expressed as follows:

$$\begin{bmatrix} \boldsymbol{G}_{\mathrm{T}} \\ \boldsymbol{G}_{\mathrm{I}} \\ \lambda \cdot \begin{pmatrix} \boldsymbol{L}_{\mathrm{t}} \\ \boldsymbol{L}_{\mathrm{s}} \end{pmatrix} \end{bmatrix} \boldsymbol{m} \cong \begin{bmatrix} \boldsymbol{d}_{\mathrm{T}} \\ \boldsymbol{d}_{\mathrm{I}} \\ \begin{pmatrix} 0 \\ 0 \end{pmatrix} \end{bmatrix}, \tag{3}$$

where $\boldsymbol{G}_{\mathrm{T}}$ and $\boldsymbol{G}_{\mathrm{I}}$ denote the Green function for teleseismic and InSAR data respectively, and λ is a scalar factor controlling the smoothing strength, which was determined by Akaike's Bayesian Information Criterion here (Akaike, 1980). The weights of the teleseismic data vector $\boldsymbol{d}_{\mathrm{T}}$ and InSAR data vector $\boldsymbol{d}_{\mathrm{I}}$ were empirically set to 1 and 0.5, respectively. Meanwhile, the weights for the interferograms and offset data were set according to their variances. $\boldsymbol{L}_{\mathrm{t}}$ and $\boldsymbol{L}_{\mathrm{s}}$ are the smoothing operations applied in the temporal and space domain.

2.3.2 Postseismic slip inversion

The postseismic mechanisms mainly include the aseismic afterslip, poroelastic rebound and viscoelastic relaxation (Liu SZ et al., 2021). According to the spatiotemporal evolution of the postseismic deformation (Figure S7), we attribute the rapid transient motion occurring at the southeast end of the main fault to the afterslip. As for the afterslip modeling, we adopted the same downsampling strategy to process the postseismic interferograms. During the inversion process, we first utilized the uniform dislocation model to fit the coseismic displacements of the second largest aftershock. The postseismic interferograms were stacked to reduce the influence of data noise (Figure S8 in the Supplementary). Then we assumed that afterslip occurs on the main fault plane of the coseismic slip model according to the deformation fields (Figures 4, S7 and S9), and constructed the linear inversion equation as follows:

$$\begin{bmatrix} \boldsymbol{d}_{\mathrm{I}} \\ 0 \end{bmatrix} = \begin{bmatrix} \boldsymbol{G}_{\mathrm{I}} \\ \lambda \boldsymbol{S}_{\mathrm{s}} \end{bmatrix} \boldsymbol{m}, \tag{4}$$

where the model parameter $\boldsymbol{m}$ of Equation (4) was determined by employing a Nonnegative Least Squares method (Lawson and Hanson, 1995). To reduce the sampling space of the model parameters and considering that both the mainshock and second largest aftershock are dominate by strike slip (Feng WP et al., 2023), we only inverted the strike-slip components for both the afterslip and the second largest aftershock.

2.4. Robustness analysis of postseismic afterslip

To test the robustness of inversion results for afterslip, we first simulated 100 sets of data noise according to the covariance function of different data sets (Table S2 in the Supplementary) and inverted the slip model for 100 times. We chose the Standard deviation (STD) of these inverted slip models as the indicator of the robustness. This process can be expressed as follows:

$$\begin{bmatrix} \boldsymbol{d}_{\mathrm{I}} + \epsilon_{\mathrm{simu}} \\ 0 \end{bmatrix} = \begin{bmatrix} \boldsymbol{G}_{\mathrm{I}} \\ \lambda \boldsymbol{S}_{\mathrm{s}} \end{bmatrix} \boldsymbol{m}_i (i = 1, \ldots, 100), \tag{5}$$

where $\boldsymbol{G}_{\mathrm{I}}$ denotes the Green function for InSAR data, and λ expresses the Laplacian smoothing factor. ϵ_{simu} denotes the simulated data noise and $\boldsymbol{m}_i$ was the derived slip model. We also chose the resolution operator as another in-

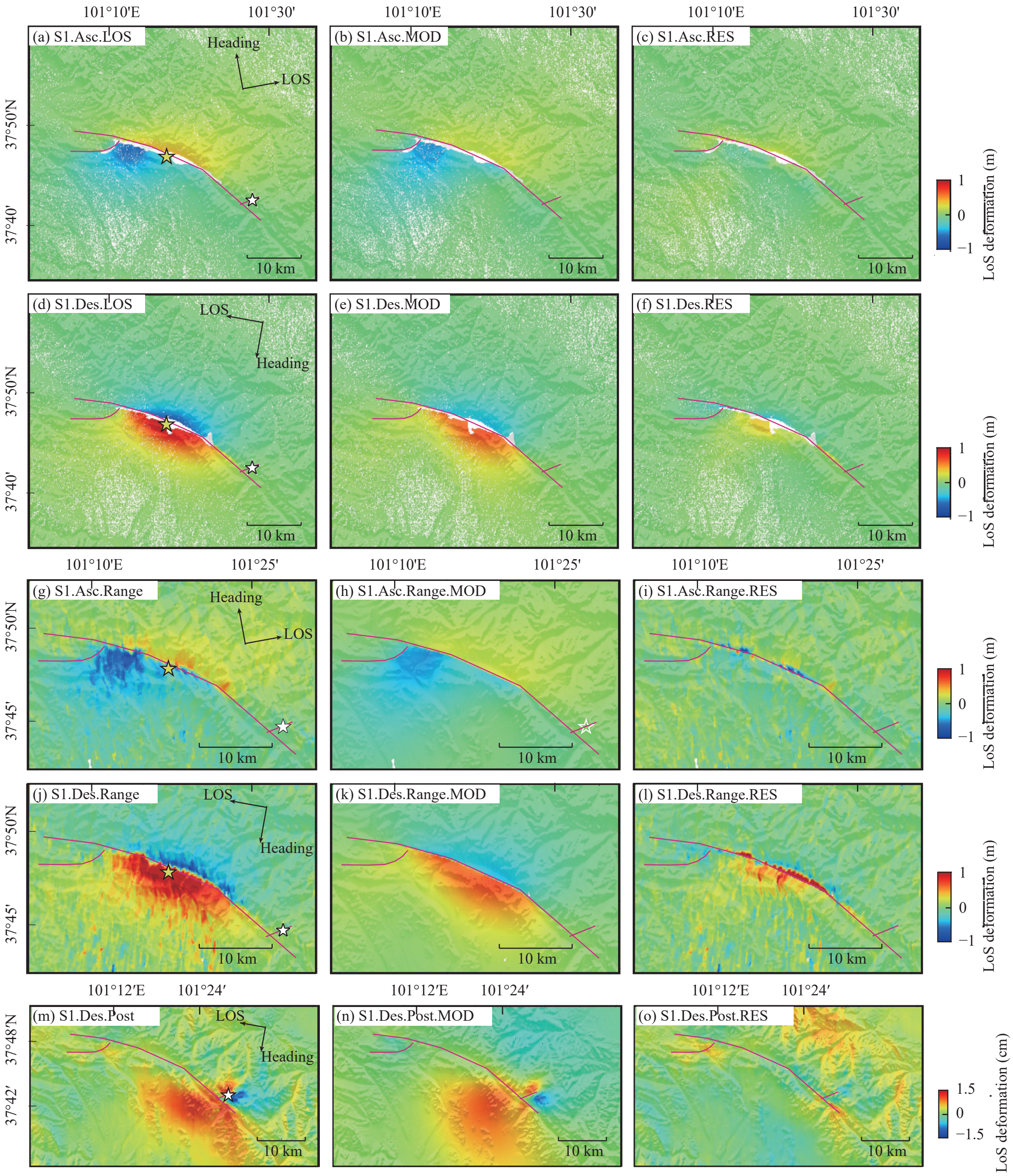

Figure 4. Coseismic and postseismic deformation fields and corresponding modeling results of 2022 Menyuan earthquake sequences. (a–c) Observed, modeled and residual of the cumulative ascending coseismic deformation. Cold color values indicate LOS/Range displacement towards the satellite. (d–f) Same with (a–c), but for the descending cumulative coseismic deformation. (g–i) indicate the observed, modeling and residual of the cumulative ascending range offset fields. (j–l) are the results of the cumulative descending range offsets field. (m–o) are the observed, modeled and residual of the cumulative descending postseismic deformation spanning from 2 days to 38 days after mainshock. Yellow and white stars represent the epicenters of the mainshock and the second largest aftershock, respectively. The magenta lines denote the fault model utilized for inversion in this study.

dicator of inversion robustness. The calculation of slip resolution $\boldsymbol{R}_\mathrm{s}$ can be expressed as follows (Jolivet et al., 2012):

$$\boldsymbol{R}_\mathrm{s} = \boldsymbol{G}^{-\mathrm{g}}\boldsymbol{G}, \tag{6}$$

where $\boldsymbol{G}$ denotes the Green function and $\boldsymbol{G}^{-\mathrm{g}}$ is the generalized inverse matrix of ***G***.

3. Results

3.1. Coseismic and postseismic deformation

From the LOS and range offsets fields of the Menyuan earthquake (Figure 4), we infer the seismogenic fault roughly distributes in the northwest-southeast direction. The fault rupture reached to the surface during the coseismic period, causing a significant deformation gradient and resulting in near-field incoherence of the coseismic interferograms. From the ascending interferogram, the deformation was found to range from −0.67 m to 0.44 m. And the deformation range is −0.71 m to 1 m in the descending interferogram. The near-field deformation recovered by the range offsets is roughly −0.6 m to 0.4m and − 0.7 m to 1 m for the ascending and descending interferograms, respectively. The opposite deformation patterns in different tracks indicates the 2022 Menyuan earthquake is dominated by a sinistral strike-slip, which is in good accordance with the regional tectonic setting.

The postseismic interferograms after correcting atmospheric delay exhibit localized postseismic signals at the southeastern part of the main fault and show a gradually increased deformation with time, which can be attributed to the time-dependent afterslip process (Figure S7 and S9). But no obvious deformation is detected near the secondary fault, which may be attributed to the possible complete rupture in deep depth, the complexity of fault geometry and the regional stress field in this region. We suggest the local double-lobe deformation signal at the north-eastern tip of the main fault is caused by the second largest M_W5.1 aftershock. According to the strike-slip focal mechanism of the second largest aftershocks that occurred on 12 January 2022 (Feng WP et al., 2023) and the corresponding deformation patterns observed in this study, we suggest the two-lobe deformation pattern is caused by dextral fault slip on a nearly conjugated secondary fault relative to the main fault.

3.2. Coseismic rupture process

As shown from our kinematic inversion result (Figure 5), the major slip occurs on the LLLF with a maximum strike-slip of 3 m and maximum dip-slip of 0.65 m. The maximum fault slip is located at depth of 4 km. The moment released by the earthquake is 1.83×10^{19} Nm (M_W6.78), which is slightly larger than M_W 6.6 of USGS and M_W 6.7 of GCMT. This could be attributed to the possible postseismic deformation included in the SAR data (Table S1 in the Supplementary) (Liu XG et al., 2022b). The sub-processes of the source rupture show that the Menyuan earthquake is a bilateral rupture event with a total ~15 s duration. The coseismic rupture starts at the LLLF and propagates to the TLSF 3 s after the rupture begins. The energy-releasing process consists of two stages. In the first stage, a large asperity is ruptured from the initiation point, and its rupture process lasts for about 10 s on the LLLF, and gradually reaching its maximum rate of seismic moment release at about 4 s. Then, the rate of seismic moment release starts to decrease but appears to rise again between 7 s and 9 s, followed by the later rate decrease of seismic moment releases again. The second stage corresponds to a small slip in the remaining area of the fault plane, which lasts about 5 s.

Most of the data from the seismic stations can be well explained by our inversion results unless the initial motion part of the P-wave data from a few teleseismic stations could not be fitted well (Figure S10). This could be attributed to the data noise. The maximum InSAR residuals appear mainly on the near field of epicentral areas (Figure 4), which may be attributed to the over-simplification of the fault geometry or the inelastic deformation caused by the earthquake. The RMS of the residuals derived from the joint model inversion are 1.95 cm and 2.60 cm in the ascending interferogram and descending interferogram, respectively. Considering the offset-tracking data area is usually noisier than the interferograms, the RMS of the residuals are 8.07 cm and 12.73 cm for the ascending and descending data, respectively.

3.3. Afterslip and the second largest aftershock

To avoid the obvious trade-off of the simultaneous inversions of the second largest aftershock and afterslip, we first determined the uniform fault model of the second largest aftershock using the local deformation induced by the second largest aftershock in postseismic interferograms (Figure S8 in the Supplementary). According to the focal mechanism by Feng WP et al. (2023) with a much minor dip-slip component, only the strike-slip component of the aftershock model is considered to reduce the model space (Table S4 in the Supplementary). The inversion result shows the aftershock occurs on a secondary fault with a strike of 242°, forming a nearly conjugate fault with the ruptured main fault. The aftershock slip reaches 0.15 m and doesn’t rupture to the surface. The released geodetic moment is ~4.63×10^{16} Nm, corresponding to an M_W5.08 earthquake. The observed deformation is well fitted by the modeling results, with the RMS of 0.26 cm for the stacked interferogram (Figure S8). The corresponding residuals likely include part of the deformation associated with the

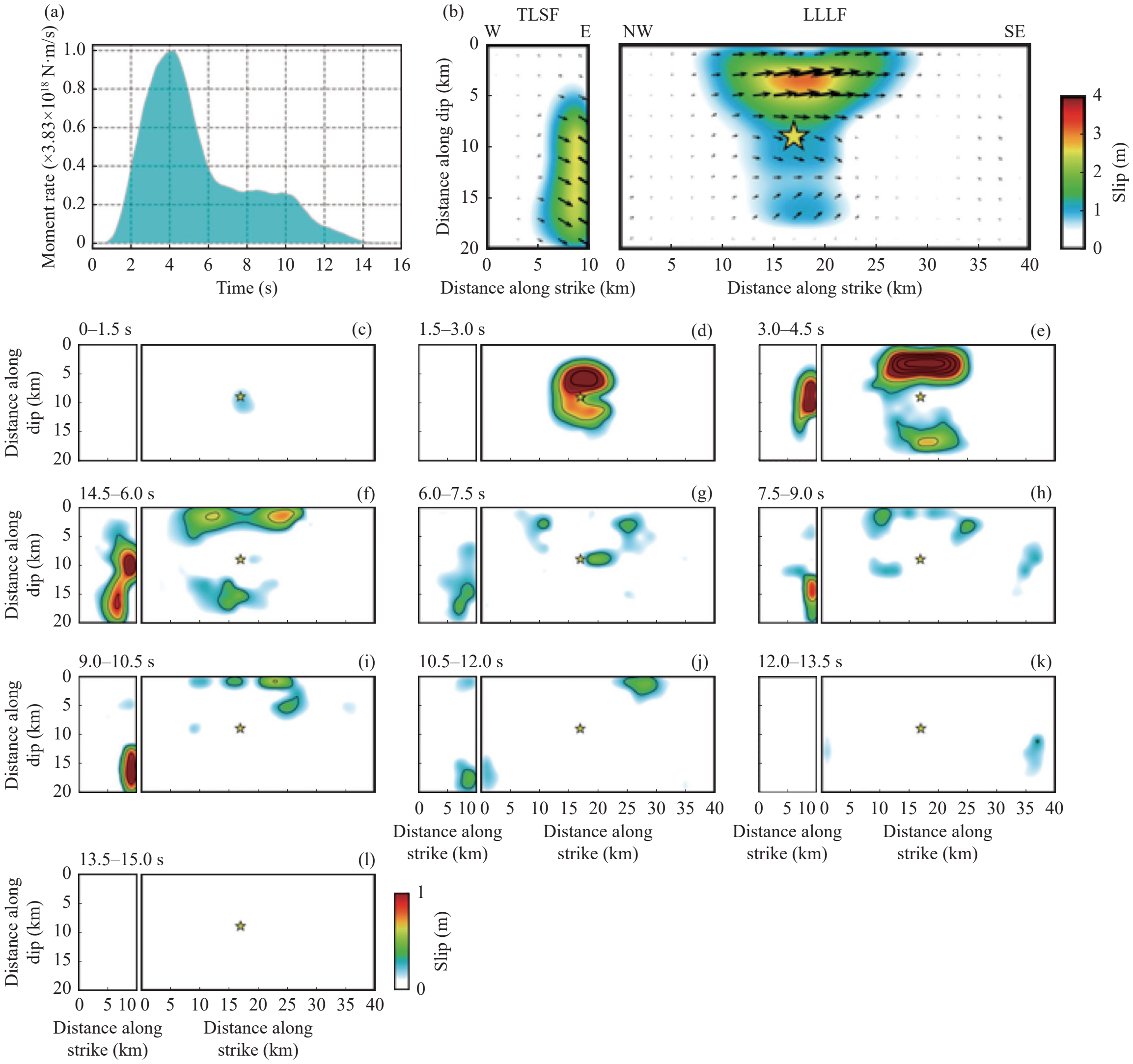

Figure 5. The kinematic rupture process of the 2022 Menyuan main shock. (a) Source time function of optimal model. (b) Final slip distribution of joint inversion. (c–l) Snapshots and final distribution of the source rupture process from optimal model. The contour of the slip distribution in (c–l) is 0.3m.

afterslip (Figure S8), which will be addressed in the later afterslip inversion. After removing the deformation signal caused by the second largest aftershock (Figure S8h), we performed the distributed afterslip inversion on the main fault (Figures 4 and S9). The inversion results show that the cumulative afterslip reaches ~0.2m after 38 days of the mainshock (Figures 6 and S11) and mainly confines at a downdip zone of coseismic slip, forming the complementarity pattern between the afterslip and the coseismic slip. The cumulative moments released by afterslip are ~4.15×10^{17} N·m, ~5.59×10^{17} N·m and ~1.14×10^{18} N·m after 14 days, 26 days and 38 days after the mainshock, corresponding to M_W5.72, M_W 5.80 and M_W6.01 earthquakes respectively (Figure S9). The modeling results fit the deformation data well and the corresponding RMS are 0.14 cm, 0.17 cm and 0.25 cm respectively (Figure S9).

The slip uncertainties and resolutions of cumulative afterslip models are analyzed (Figures 6 and S12). The slip uncertainties are generally smaller for the shallow region than the deeper part of the fault, suggesting the observations have better constraining ability on shallow fault regions than the deeper fault regions. Part of the high slip uncertainty area overlapped with our afterslip models on the downdip part of the mainshock, but they are much smaller than the derived maximum afterslip. The resolutions also show the data have enough resolving power on most of the fault patches, except the deepest part of the fault model. The robustness of the afterslip models is thus confirmed by both slip uncertainties and resolutions analysis.

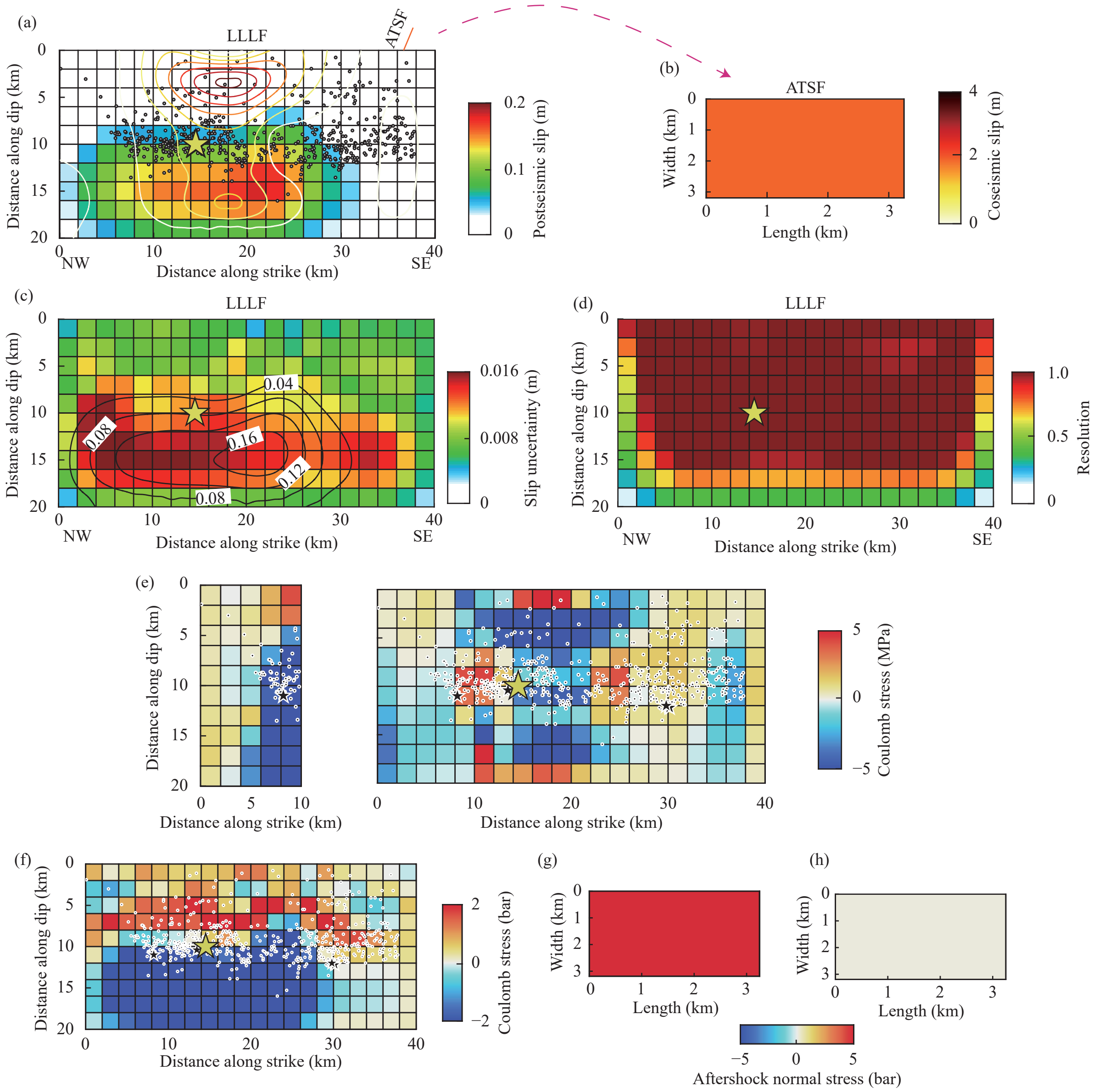

Figure 6. The spatial relationship among coseismic slip, afterslip, and aftershocks, along with stress perturbations analysis. (a) represents the afterslip model corresponding to 38 days after the mainshock. (b) represents the uniform slip model of the second largest aftershock. Note that the colorbars for (a) and (b) are different. (c) and (d) represent the slip uncertainty and slip resolution of the afterslip model corresponding to 38 days after the mainshock. The yellow stars represent the epicenter of the mainshock. The gray dots denote the relocated aftershocks. The smoothed contour lines with 0.5 m intervals in (a) are coseismic slip models. The smoothed contour lines with 0.04 m interval in (c) are postseismic afterslip model. (e) represents the static Coulomb stress change on the seismogenic fault surface induced by coseismic slip and (f) represents the Coulomb stress change caused by afterslip corresponding to 38 days after mainshock. The normal stress change on the conjugated fault of the second largest aftershock induce by the (g) coseismic slip and (h) afterslip 14 days after the mainshock, and the positive normal stress change indicate the transtensional effect of the conjugated fault. The black stars in (e) and (f) represent the larger aftershocks (M>4.0). Other smaller aftershocks are denoted by white dots in (e) and (f).

4. Discussion

4.1. Comparison of different coseismic slip models

In the comparative analysis of my slip model with four representative models (Feng WP et al., 2023; He LJ et al., 2024; Lü MZ et al., 2022; Luo H and Wang T, 2022) in terms of fault geometry, slip magnitude, and slip distribution, Feng WP et al. (2023) proposed a model with two curved fault surfaces, featuring dip angles of 70° and 88° determined based on relocated aftershocks. Luo H and Wang T (2022) constructed a fault model with multiple straight segments. He LJ et al. (2024) utilized a model with two curved fault surfaces constructed through triangular dislocations, with patch sizes increasing with depth. In contrast to the formal analysis based on InSAR observations, Lü MZ et al. (2022) conducted inversion work based on both high-frequency GNSS displacement waveforms and InSAR data, employing two simplified planar faults for modeling with the same dip angles of 80°.

In this study, we constructed a fault model consisting of two curved fault surfaces based on the range offset fields, and then determined the dip angle of the fault through nonlinear inversion to be 79°. Concerning slip magnitude, Feng WP et al. (2023); He LJ et al. (2024) reported maximum slips of approximately 3 m at a depth of around 4 km, while Luo and Lü MZ et al. (2022) inferred maximum slip magnitudes of 3.6 m and ~4 m, respectively.

The slip distribution was obtained through the joint inversion of InSAR data and teleseismic data in this study, with the maximum slip determined to be 3 m. Regarding slip distribution, although all models exhibit two slip asperities on the ruptured faults, variations in slip characteristics emerge on the Tuolaishan fault segment. Feng WP et al. (2023); Luo H and Wang T (2022) identified strike-slip motion in the TLSF, while Lü MZ et al. (2022) additionally recognized a reverse motion on this fault. He LJ et al. (2024) found a normal faulting component in the TLS fault. Our study suggests the presence of a normal faulting component in this segment as well, along with a small reverse faulting component in the LLLF, possibly related to a pull-apart stress field in the following analysis. Many factors, such as fault geometry simplification, data selection and smoothing factors, may impact the inversion results. The model comparisons here do not aim to assert superiority but seek to further understand the uncertainties in inversion. It highlights the importance of seismic source modeling in understanding the rupture process of the Menyuan earthquake.

4.2. Interplay between the afterslip, coseismic slip and aftershocks

By comparing the afterslip, coseismic slip and aftershocks associated with the 2022 Menyuan earthquake, we find the complementary characteristics between the afterslip and coseismic slip (Figures 6 and S11). The aseismic afterslip mainly occurred in the downdip direction of the mainshock ruptured area, illuminating the possible velocity-strengthening behavior in the deep section of the fault. Recent seismological researches also proved that Menyuan earthquake happened on the boundary between the high and low velocity zones (Sun AH et al., 2022; Xu YC et al., 2022). Meanwhile, the slip on the branch shows some normal components, indicating the TLS dives to the deep part of the LLL fault, which can be evidenced by the small normal-slip component in the deep LLL fault (Figure 5). This may be explained by a small-pull apart basin formed by the LLL and TLS faults, causing the heterogeneous stress in this area. In addition, one potential reason for the deep slip distribution on TLSF can also be attributed to the high-velocity anomaly zone existing in the deep part of this region as suggested by Xu YC et al. (2022), which could behave as a slip barrier before the Menyuan earthquake and thus hold higher stress.

In all, the Menyuan mainshock mainly ruptured the position of two primary asperities, while the afterslip mainly occurs in the deep region on the southeastern section of the main fault. According to the stress-driven afterslip model, the coseismic and postseismic slip should not overlap. The partially overlapped coseismic slip and afterslip in this study may be explained by the smoothed constraint, the possible redistribution of shallow material or the stress reorganization following the significant coseismic slip (He LJ et al., 2021).

The calculated Coulomb stress change shows the maximum stress change reaches 5 MPa around the major slip area on the ruptured fault (Figure 6). Additionally, 324 out of 563 aftershocks are located in the positive Coulomb stress area, demonstrating a good correlation of the aftershocks distribution with the stress perturbation caused by the coseismic slip. A similar correlation can also be observed in the stress perturbation induced by postseismic slip, where 262 out of 563 aftershocks are situated in the positive stress region. This suggests that stress redistribution following the mainshock may have impact on the distribution of aftershocks as well (Figure S13). Possible explanations for aftershocks in the stress shadow could be the location error of aftershocks, the oversimplification of the seismogenic fault and the modeling error of slip.

4.3. Conjugated rupturing of the second largest aftershock

The Menyuan earthquake reveals a complex fault system and regional stress field around the LLLF and TLSF area. According to the modeling results, rapid postseismic transient motion follows the Menyuan mainshock, releasing ~88% energy of coseismic slip one month after the mainshock. Interestingly, a branch fault is ruptured during the second largest aftershock four days after the mainshock, forming a nearly conjugate fault system. Such high-angle rupture earthquake sequence happens rarely but exists in other earthquake events, such as the 2019 Mindanao and Ridgecrest earthquake sequences (Barnhart et al., 2019; Zhao L et al., 2021). According to the Mohr-Coulomb criterion, the angle between two ruptured faults depends on the rock strength, and two conjugated faults hardly ruptured at the same time with a friction coefficient normally being 0.6–0.7 (Collettini and Sibson, 2001).

Recent studies attribute this rare phenomenon to heterogeneous fault rock strength, the time-dependent fault weakening and insufficient prior knowledge of the fault strength (Wang KL, 2021). However, there are still great controversies about high-angle ruptured earthquake sequences. As for the 2019 Ridgecrest earthquake sequence, Liang C et al. (2021) proposed a faulting model with a ductile deeper layer and a brittle upper layer, leading to the conjugate rupture gradually propagating from a deep part to the shallow surface. While Fialko and Jin ZY (2021) proposed that conjugated fault systems around Ridgecrest area were formed during the gradual rotation of the regional faults caused by the long-term tectonic deformation and a shear stress orientating ~45° concerning the principle compression axis of this region.

To probe the role of local stress in the conjugate rupture during the 2022 Menyuan earthquake sequence, we compiled a database of fault plane solutions including 23 focal mechanisms during 2009–2019 time-interval from the National Earthquake Data Center (https://data.earthquake.cn, 2022. DOI: 10.12080/nedc.11.ds.2022.0004) and the mainshock mechanism derived in this study (Figure 1a, Tables S5, S6) to estimate the local stress field. Then, we adopted an iterative stress inversion method to calculate triaxial stress field σ_1, σ_2, σ_3 and the stress shape ratio $R=(\sigma_1-\sigma_2)/(\sigma_1-\sigma_3)$ (Liu XG et al., 2022a; Vavryčuk, 2014). The average misfit angle α=15.8° describes the difference between the predicted and observed fault slip directions (Figure S14), and this small misfit angle indicates the relatively homogeneous local stress field (Liu XG et al., 2022b). The azimuth direction of maximum compression stress is ~222°, forming an angle of 22° with the strike direction of the ruptured conjugate fault hosting the second largest aftershock.

According to the dynamical simulation research by Lozos (2022), the conjugated fault of the second largest aftershock was significantly more favorable than the main fault in this situation. Besides, recent dynamic simulation studies suggest the reduction of normal stress will promote the rupture of the conjugated fault system, indicating that the high-angle faulting is more prone to happen in a tensile stress field than in a compressional tectonics. This is confirmed by the normal stress shadow in the location of the second largest aftershock, induced by both our coseismic slip and afterslip. According to the studies of two historic earthquakes that happens near Menyuan (Wang H et al., 2017), there is a pull-apart basin near Menyuan. The second largest aftershock of the 2022 Menyuan earthquake sequence is near the transtensional part of the pull-apart basin (Figure 1) suggesting that the pull-apart basin favors this conjugate faulting event. Based on the above analyses, we suggest the local stress field combined with the influence of coseismic and postseismic slip, plays an important role in triggering the second largest aftershock that occurred on conjugated fault. This understanding is crucial for comprehending conjugated fault ruptures in other regions.

4.4. Implication for regional seismic risk

The Tianzhu seismic gap is a ~250 km long seismic silent region, with the capability of holding devastating earthquakes, and has been the focus of studying the seismic risk (Cavalié et al., 2008). The 2022 M_W6.7 Menyuan earthquake occurred at the western end of the Tianzhu seismic gap. It partially ruptured the TLSF, the LLLF, and a high-angle conjugated fault at the northeastern part of the main fault. The decline slip propagation towards the surface is related to hypocenter-dependent effects (Yao SL and Yang HF, 2022), and the partial release of accumulated interseismic strain may indicate the future seismic risk. Meanwhile, the geometrical complexities of the regional fault system, especially the conjugated rupturing, and the regional stress field possibly limit the further lateral propagation of the 2022 Menyuan earthquake.

Considering that there is ~200 km long silent region, the seismogenic capacity of this region is still high and it's crucial for us to evaluate the regional seismic risk. To infer the possible triggering effect between the 2022 Menyuan earthquake and the Tianzhu seismic gap, we utilized the friction coefficient of 0.4 to calculate the Coulomb stress change induced by the coseismic slip, afterslip and the second largest aftershock. The source fault parameters during the CSC calculation were set according to our model results. The receiver fault parameters were set according to the fault parameters of the Lenglongling fault, and were also consistent with our modeling results for the mainshock here. The CSC induced by the mainshock and second largest aftershock reaches 1.9 MPa at the epicentral area and ~0.05 MPa at the western side of the Tianzhu seismic gap (Figure 7), indicating the significant triggering effect and the potential increase of seismic risk in Tianzhu seismic gap. In addition, during the postseismic process following the 2022 Menyuan mainshock, the maximum

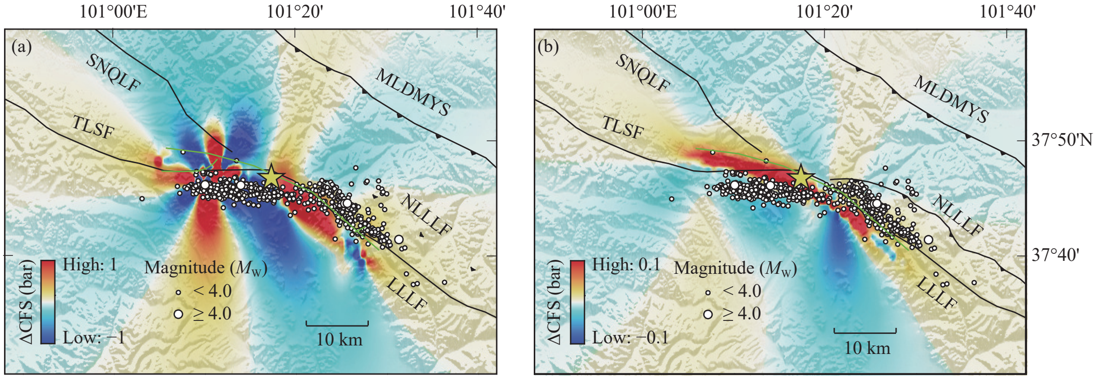

Figure 7. Coulomb stress change induced by the (a) mainshock, as well as the largest aftershock and (b) the afterslip 36 days after the mainshock. The Coulomb stress modeling is at 20 km depth with the receiver fault parameters determined by our inversion results. The relocated aftershocks are denoted by white dots.

CSC induced by afterslip is ~0.07 MPa near the epicentral area and ~0.001 MPa on the western Tianzhu seismic gap.

Although the triggering effect induced by the afterslip is smaller relative to the coseismic influence, it is hard to rule out the promotion of postseismic processes to trigger future large earthquake on the Tianzhu seismic gap, especially when we consider a long-term postseismic period. The coseismic slip and the second largest aftershock have loaded the stress on the TLSF with the CSC reaching ~0.02 MPa, while the afterslip induces the stress unloading on TLSF with CSC of ~−0.001 MPa. As the commonly known earthquake-triggering threshold of 0.01 MPa (Ziv and Rubin, 2000), it is crucial to pay attention to the future seismic risk of this area.

5. Conclusions

The 2022 M_W 6.7 Menyuan earthquake stroke the LLLF and TLSF at the western end of the Tianzhu seismic gap. The coseismic and postseismic deformation field and slip models were studied. According to the inversion results, the mainshock ruptured bilaterally and is dominated by sinistral slip. The afterslip mainly occurred on the downdip of the coseismic rupture area, forming a complementary characteristics with the coseismic slip. The relationship between static Coulomb stress change and distribution of aftershocks indicates the aftershocks are triggered by the coseismic slip and afterslip. The stress inversion results indicate the maximum principal stress direction of ~222°, forming a ~22° angle with the ruptured fault by the second largest aftershock. The kind of conjugated is found to be compatible with the regional stress field according to the dynamical simulation research. The normal stress reduction induced by the coseismic and postseismic slip was also found to provide the tensile stress environment and favor the conjugated rupturing. The CSCs induced by the coseismic slip, afterslip and the second largest aftershock promote the seismic risk on Tianzhu seismic gap. This study will improve our understanding of the regional seismic risk and the conjugated faulting origins in other regions.

Acknowledgement

This research was supported by the National Science Fund for Distinguished Young Scholars (No. 41925016), National Key Research and Development Program (No. 2022YFB3903602), National Natural Science Foundation of China (No. 42174023) and the Frontier Cross Research Project of Central South University (No. 2023QYJC006). Copernicus data from the Sentinel-1 satellite constellation provided by the European Space Agency (https://scihub.copernicus.eu). Several figures were prepared using the Generic Mapping Tools software (Wessel et al., 2013).

Conflict of interest

Prof. Wenbin Xu serves as an editorial board member for *Earthquake Science* and was not involved in the editorial review or the decision-making process for this article. All authors declare that they have no competing interests.

References

Akaike H (1980). Likelihood and the Bayes procedure. Trab Estad Invest Oper **31**(1): 143–166. https://doi.org/10.1007/BF02888350.

Aki K and Richards PG (2002). Quantitative Seismology. 2nd ed.

University Science, Sausalito.

Bao X, Zhang R, Wang T, Shama A, Zhan RQ, Lv JC, Wu RZ, Fu Y and Liu GX (2022). The source mechanism and fault movement characterization of the 2022 M_W 6.7 menyuan earthquake revealed by the joint inversion with InSAR and teleseismic observations. Front Environ Sci **10**: 917042. https://doi.org/10.3389/fenvs.2022.917042.

Barnhart WD, Hayes GP and Gold RD (2019). The July 2019 Ridgecrest, California, earthquake sequence: kinematics of slip and stressing in cross-fault ruptures. Geophys Res Lett **46**(21): 11859–11867. https://doi.org/10.1029/2019GL084741.

Cavalié O, Lasserre C, Doin MP, Peltzer G, Sun J, Xu X and Shen ZK (2008). Measurement of interseismic strain across the Haiyuan fault (Gansu, China), by InSAR. Earth Planet Sci Lett **275**(3-4): 246–257. https://doi.org/10.1016/j.epsl.2008.07.057.

Chen CW and Zebker HA (2001). Two- dimensional phase unwrapping with use of statistical models for cost functions in nonlinear optimization. J Opt Soc Am A **18**(2): 338–351. https://doi.org/10.1364/JOSAA.18.000338.

Collettini C and Sibson RH (2001). Normal faults, normal friction. ? Geology **29**(10): 927–930. https://doi.org/10.1130/0091-7613(2001)029<0927:NFNF>2.0.CO;2.

Elliott JR, Biggs J, Parsons B and Wright TJ (2008). InSAR slip rate determination on the Altyn Tagh Fault, northern Tibet, in the presence of topographically correlated atmospheric delays. Geophys Res Lett **35**(12): L12309. https://doi.org/10.1029/2008GL033659.

Fan LP, Li BR, Liao SR, Jiang C and Fang LH (2022). High-precision relocation of the aftershock sequence of the January 8, 2022, M_S6.9 Menyuan earthquake. Earthq Sci **35**(2): 138–145. https://doi.org/10.1016/j.eqs.2022.01.021.

Farr TG, Rosen PA, Caro E, Crippen R, Duren R, Hensley S, Kobrick M, Paller M, Rodriguez E, Roth L, Seal D, Shaffer S, Shimada J, Umland J, Werner M, Oskin M, Burbank D and Alsdorf D (2007). The shuttle radar topography mission. Rev Geophys **45**(2): RG2004. https://doi.org/10.1029/2005RG000183.

Feng WP, He XH, Zhang YP, Fang LH, Sergey S and Zhang PZ (2023). Seismic faults of the 2022 M_W6.6 Menyuan, Qinghai earthquake and their implication for the regional seismogenic structures. Chin Sci Bull **68**(2-3): 254–270 . https://doi.org/10.1360/TB-2022-0154 (in Chinese with English abstract).

Fialko Y and Jin ZY (2021). Simple shear origin of the cross-faults ruptured in the 2019 Ridgecrest earthquake sequence. Nat Geosci **14**(7): 513–518. https://doi.org/10.1038/s41561-021-00758-5.

Gao H, Liao MS and Feng GC (2021). An improved quadtree sampling method for InSAR seismic deformation inversion. Remote Sens **13**(9): 1678. https://doi.org/10.3390/rs13091678.

Gaudemer Y, Tapponnier P, Meyer B, Peltzer G, Guo SM, Chen ZT, Dai HG and Cifuentes I (1995). Partitioning of crustal slip between linked, active faults in the eastern Qilian Shan and evidence for a major seismic gap, the ‘Tianzhu gap’, on the western Haiyuan Fault, Gansu (China). Geophys J Int **120**(3): 599–645. https://doi.org/10.1111/j.1365-246X.1995.tb01842.x.

Goldstein RM and Werner CL (1998). Radar interferogram filtering for geophysical applications. Geophys Res Lett **25**(21): 4035–4038. https://doi.org/10.1029/1998GL900033.

Han LF, Liu-Zeng J, Yao WQ, Shao YX, Yuan ZD and Wang Y (2021). Coseismic slip gradient at the western terminus of the 1920 Haiyuan M_W7.9 earthquake. J Struct Geol **152**: 104442. https://doi.org/10.1016/j.jsg.2021.104442.

Han S, Wu ZH, Gao Y and Lu HF (2022). Surface rupture investigation of the 2022 Menyuan M_S 6.9 earthquake, Qinghai, China: implications for the fault behavior of the Lenglongling fault and regional intense earthquake risk. J Geomech **28**(2): 155–168 . https://doi.org/10.12090/j.issn.1006-6616.2022013 (in Chinese with English abstract).

He LJ, Feng GC, Wu XX, Lu H, Xu WB, Wang YD, Liu JH, Hu J and Li ZW (2021). Coseismic and early postseismic slip models of the 2021 M_W 7.4 Maduo earthquake (western China) estimated by space-based geodetic data. Geophys Res Lett **48**(24): e2021GL095860. https://doi.org/10.1029/2021GL095860.

He LJ, Feng GC, Wang YD, Xiong ZQ, Gao H and Liu XG (2024). Geodetic source models of the 2016–2022 Menyuan Earthquake sequence (Northeastern Tibet) inferred from InSAR and optical observations. Geophys J Int **236**(1): 470–479. https://doi.org/10.1093/gji/ggad429.

Huang ZC, Zhou Y, Qiao X, Zhang PZ and Cheng X (2022). Kinematics of the ~1000 km Haiyuan fault system in northeastern Tibet from high-resolution Sentinel-1 InSAR velocities: fault architecture, slip rates and partitioning. Earth Planet Sci Lett **583**: 117450. https://doi.org/10.1016/j.epsl.2022.117450.

Ji ZW, Li ZC, Gao MT, Sun JZ and Guo XY (2022). Simulation of strong earthquake characteristics of a scenario earthquake (M_S7.5) based on the enlightenment of 2022 M_S6.9

earthquake in Menyuan. Earthq Sci **35**(6): 485–496. https://doi.org/10.1016/j.eqs.2022.11.001.

Jolivet R, Lasserre C, Doin MP, Guillaso S, Peltzer G, Dailu R, Sun J, Shen ZK and Xu X (2012). Shallow creep on the Haiyuan fault (Gansu, China) revealed by SAR interferometry. J Geophys Res: Solid Earth **117**(B6): B06401. https://doi.org/10.1029/2011JB008732.

Lasserre C, Morel PH, Gaudemer Y, Tapponnier P, Ryerson FJ, King GCP, Métivier F, Kasser M, Kashgarian M, Liu BC, Lu TY and Yuan DY (1999). Postglacial left slip rate and past occurrence of $M \geq 8$ earthquakes on the Western Haiyuan Fault, Gansu, China. J Geophys Res: Solid Earth **104**(B8): 17633–17651. https://doi.org/10.1029/1998jb900082.

Lawson CL and Hanson RJ (1995). Solving Least Squares Problems. SIAM, Philadelphia, pp 158-173.

Li YS, Jiang WL, Li YJ, Shen WH, He ZT, Li BQ, Li Q, Jiao QS and Tian YF (2022). Coseismic rupture model and tectonic implications of the January 7 2022, Menyuan M_W6.6 earthquake constraints from InSAR observations and field investigation. Remote Sens **14**(9): 2111. https://doi.org/10.3390/rs14092111.

Liang C, Ampuero JP and Pino Muñoz D (2021). Deep ductile shear zone facilitates near-orthogonal strike-slip faulting in a thin brittle lithosphere. Geophys Res Lett **48**(2): e2020GL090744. https://doi.org/10.1029/2020GL090744.

Liu HZ, Xie L, Zhao GQ, Ali E and Xu WB (2023). A joint InSAR-GNSS workflow for correction and selection of interferograms to estimate high-resolution interseismic deformations. Satell Navig **4**(1): 14. https://doi.org/10.1186/s43020-023-00105-6.

Liu JH, Hu J, Li ZW, Ma ZF, Shi JW, Xu WB and Sun Q (2022). Three-dimensional surface displacements of the 8 January 2022 M_W 6.7 Menyuan Earthquake, China from Sentinel-1 and ALOS-2 SAR observations. Remote Sens **14**(6): 1404. https://doi.org/10.3390/rs14061404.

Liu SZ, Shen ZK, Bürgmann R and Jónsson S (2021). Thin crème brûlée rheological structure for the Eastern California Shear Zone. Geology **49**(2): 216–221. https://doi.org/10.1130/g47729.1.

Liu XG, Xu WB, He ZL, Fang LH and Chen ZD (2022a). Aseismic slip and cascade triggering process of foreshocks leading to the 2021 M_W6.1 Yangbi Earthquake. Seismol Res Lett **93**(3): 1413–1428. https://doi.org/10.1785/0220210263.

Liu XG, Xu WB, Radziminovich NA, Fang N and Xie L (2022b). Transtensional coseismic fault slip of the 2021 M_W6.7 Turt Earthquake and heterogeneous tectonic stress surrounding the Hovsgol Basin, Northwest Mongolia. Tectonophysics **836**: 229407. https://doi.org/10.1016/j.tecto.2022.229407.

Liu-Zeng J, Klinger Y, Xu XW, Lasserre C, Chen GH, Chen WB, Tapponnier P and Zhang B (2007). Millennial recurrence of large earthquakes on the Haiyuan fault near Songshan, Gansu Province, China. Bull Seismol Soc Am **97**(1B): 14–34. https://doi.org/10.1785/0120050118.

Lozos JC (2022). Dynamic rupture modeling of coseismic interactions on orthogonal strike-slip faults. Geophys Res Lett **49**(5): e2021GL097585. https://doi.org/10.1029/2021GL097585.

Lü MZ, Chen KJ, Chai HS, Geng JH, Zhang SP and Fang LH (2022). Joint inversion of InSAR and high-rate GNSS displacement waveforms for the rupture process of the 2022 Qinghai Menyuan M6.9 earthquake. Chin J Geophys **65**(12): 4725–4738. https://doi.org/10.6038/cjg2022Q0304 (in Chinese with English abstract).

Luo H and Wang T (2022). Strain partitioning on the western Haiyuan fault system revealed by the adjacent 2016 M_W5.9 and 2022 M_W 6.7 Menyuan earthquakes. Geophys Res Lett **49**(16): e2022GL099348. https://doi.org/10.1029/2022GL099348.

Métivier F, Gaudemer Y, Tapponnier P and Meyer B (1998). Northeastward growth of the Tibet plateau deduced from balanced reconstruction of two depositional areas: the Qaidam and Hexi Corridor basins, China. Tectonics **17**(6): 823–842. https://doi.org/10.1029/98tc02764.

Michel R, Avouac JP and Taboury J (1999). Measuring ground displacements from SAR amplitude images: application to the Landers earthquake. Geophys Res Lett **26**(7): 875–878. https://doi.org/10.1029/1999GL900138.

Murray KD, Lohman RB and Bekaert DPS (2021). Cluster-based empirical tropospheric corrections applied to InSAR time series analysis. IEEE Trans Geosci Remote Sens **59**(3): 2204–2212. https://doi.org/10.1109/TGRS.2020.3003271.

Okada Y (1985). Surface deformation due to shear and tensile faults in a half-space. Bull Seismol Soc Am **75**(4): 1135–1154. https://doi.org/10.1785/BSSA0750041135.

Ou Q, Kulikova G, Yu J, Elliott A, Parsons B and Walker R (2020). Magnitude of the 1920 Haiyuan earthquake reestimated using seismological and geomorphological methods. J Geophys Res:Solid Earth **125**(8): e2019JB019244. https://doi.org/10.1029/2019JB019244.

Scheiber R and Moreira A (2000). Coregistration of interferometric SAR images using spectral diversity. IEEE Trans Geosci Remote Sens **38**(5): 2179–2191. https://doi.

org/10.1109/36.868876.

Shao YX, Liu-Zeng J, Van der Woerd J, Klinger Y, Oskin ME, Zhang JY, Wang P, Wang PT, Wang W and Yao WQ (2021). Late Pleistocene slip rate of the central Haiyuan fault constrained from optically stimulated luminescence, 14C and cosmogenic isotope dating and high-resolution topography. GSA Bull **133**(7-8): 1347–1369. https://doi.org/10.1130/B35571.1.

Simons M, Fialko Y and Rivera L (2002). Coseismic deformation from the 1999 M_W7.1 Hector Mine, California, earthquake as inferred from InSAR and GPS observations. Bull Seismol Soc Am **92**(4): 1390–1402. https://doi.org/10.1785/0120000933.

Sun AH, Gao Y, Zhao GF, Ren C and Liang SS (2022). Seismic structure and *b*-value in the focal area of the 8th January 2022 Menyuan, Qinghai M_S6.9 earthquake. Chin J Geophys **65**(3): 1175–1183. https://doi.org/10.6038/cjg2022Q0030 (in Chinese with English abstract).

Vasyura-Bathke H, Dettmer J, Steinberg A, Heimann S, Isken MP, Zielke O, Mai PM, Sudhaus H and Jónsson S (2020). The Bayesian earthquake analysis tool. Seismol Res Lett **91**(2A): 1003–1018. https://doi.org/10.1785/0220190075.

Vavryčuk V (2014). Iterative joint inversion for stress and fault orientations from focal mechanisms. Geophys J Int **199**(1): 69–77. https://doi.org/10.1093/gji/ggu224.

Wang H, Liu-Zeng J, Ng AHM, Ge L, Javed F, Long F, Aoudia A, Feng J and Shao Z (2017). Sentinel-1 observations of the 2016 Menyuan earthquake: a buried reverse event linked to the left-lateral Haiyuan fault. Int J Appl Earth Obs Geoinf **61**: 14–21. https://doi.org/10.1016/j.jag.2017.04.011.

Wang KL (2021). On the strength of subduction megathrusts. Chin J Geophys **64**(10): 3452–3465 . https://doi.org/10.6038/cjg2021P0515 (in Chinese with English abstract).

Wang WT, Zhang PZ, Garzione CN, Liu CC, Zhang ZQ, Pang JZ, Wang YZ, Zheng DW, Zheng WJ and Zhang HP (2022). Pulsed rise and growth of the Tibetan Plateau to its northern margin since ca. 30 Ma. Proc Natl Acad Sci USA **119**(8): e2120364119. https://doi.org/10.1073/pnas.2120364119.

Wessel P, Smith WHF, Scharroo R, Luis J and Wobbe F (2013). Generic mapping tools: improved version released. Eos, Trans Am Geophys Union **94**(45): 409–410. https://doi.org/10.1002/2013EO450001.

Wu XX, Feng GC, He LJ and Lu H (2023). High precision coseismic deformation monitoring method based on time-series InSAR analysis. Rev Geophys Planet Phys **54**(6): 612–621. https://doi.org/10.19975/j.dqyxx.2022-023 (in Chinese with English abstract).

Xu WB (2017). Finite-fault slip model of the 2016 M_W7.5 Chiloé earthquake, southern Chile, estimated from Sentinel-1 data. Geophys Res Lett **44**(10): 4774–4780. https://doi.org/10.1002/2017GL073560.

Xu YC, Guo XY and Feng LL (2022). Relocation and focal mechanism solutions of the M_S 6.9 Menyuan earthquake sequence on January 8, 2022 in Qinghai Province. Acta Seismol Sin **44**(2): 195–210. https://doi.org/10.11939/jass.20220008 (in Chinese with English abstract).

Yang HF, Wang D, Guo RM, Xie MY, Zang Y, Wang Y, Yao Q, Cheng C, An YR and Zhang YY (2022). Rapid report of the 8 January 2022 M_S6.9 Menyuan earthquake, Qinghai, China. Earthq Res Adv **2**(1): 100113. https://doi.org/10.1016/j.eqrea.2022.100113.

Yao SL and Yang HF (2022). Hypocentral dependent shallow slip distribution and rupture extents along a strike-slip fault. Earth Planet Sci Lett **578**: 117296. https://doi.org/10.1016/j.epsl.2021.117296.

Yin A and Harrison TM (2000). Geologic evolution of the Himalayan-Tibetan orogen. Annu Rev Earth Planet Sci **28**: 211–280. https://doi.org/10.1146/annurev.earth.28.1.211.

Yu C, Penna NT and Li ZH (2017). Generation of real-time mode high-resolution water vapor fields from GPS observations. J Geophys Res Atmos **122**(3): 2008–2025. https://doi.org/10.1002/2016JD025753.

Zhang PZ, Shen ZK, Wang M, Gan WJ, Bürgmann R, Molnar P, Wang Q, Niu ZJ, Sun JZ, Wu JC, Sun HR and You XZ (2004). Continuous deformation of the Tibetan Plateau from global positioning system data. Geology **32**(9): 809–812. https://doi.org/10.1130/g20554.1.

Zhang PZ, Min W, Deng QD and Mao FY (2005). Paleoearthquake rupture behavior and recurrence of great earthquakes along the Haiyuan fault, northwestern China. Sci China Ser D Earth Sci **48**(3): 364–375. https://doi.org/10.1360/02yd0464.

Zhao L, Qu CY, Shan XJ, Zhao DZ, Gong WY and Li YC (2021). Coseismic deformation and multi-fault slip model of the 2019 Mindanao earthquake sequence derived from Sentinel-1 and ALOS-2 data. Tectonophysics **799**: 228707. https://doi.org/10.1016/j.tecto.2020.228707.

Zheng WJ, Zhang PZ, He WG, Yuan DY, Shao YX, Zheng DW, Ge WP and Min W (2013). Transformation of displacement between strike-slip and crustal shortening in the northern margin of the Tibetan Plateau: evidence from decadal GPS measurements and late Quaternary slip rates on faults.

Tectonophysics **584**: 267–280. https://doi.org/10.1016/j.tecto.2012.01.006.

Ziv A and Rubin AM (2000). Static stress transfer and earthquake triggering: no lower threshold in sight? J Geophys Res: Solid Earth **105**(B6): 13631–13642. https://doi.org/10.1029/2000JB900081.

Supplementary

Figures showing postseismic interferograms after atmospheric delay correction (Figure S1), atmospheric delay derived by different methods (Figure S2), height versus phase plot for postseismic interferograms (Figure S3), clustering results and linear function coefficients maps (Figure S4), *L*-bow curve and semivariances plots (Figure S5), the subsampled InSAR and range offsets data (Figure S6), the raw, modeled and residual data of the postseismic interferograms, the largest aftershock and the afterslip (Figures S7, S8 and S9), the modeling results of the seismic data (Figures S10), the afterslip models corresponding to 14 days, 26 days, and 38 days after mainshock (Figures S11), the slip uncertainties and resolution matrix (Figure S12), the static coulomb stress caused by the afterslip models (Figure S13) and the stress inversion results (Figure S14).

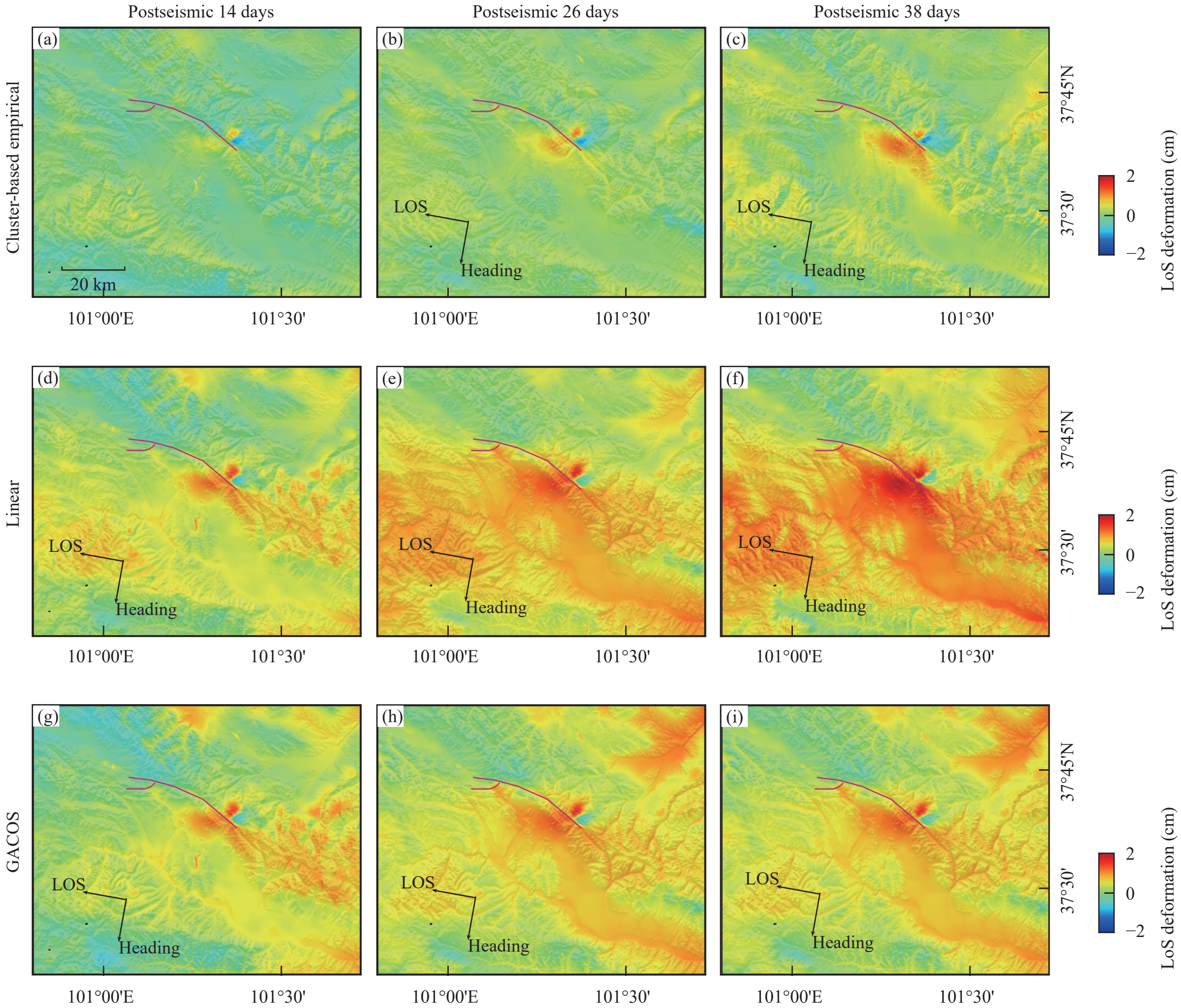

Figure S1. Postseismic LOS displacement after atmospheric delay correction. (a–c) interferograms corrected by *K*-means clustering method, (d–f) interferograms corrected by linear function, and (g–i) interferograms corrected by GACOS. Note that the dates of the interferograms are consistent with Figure S2.

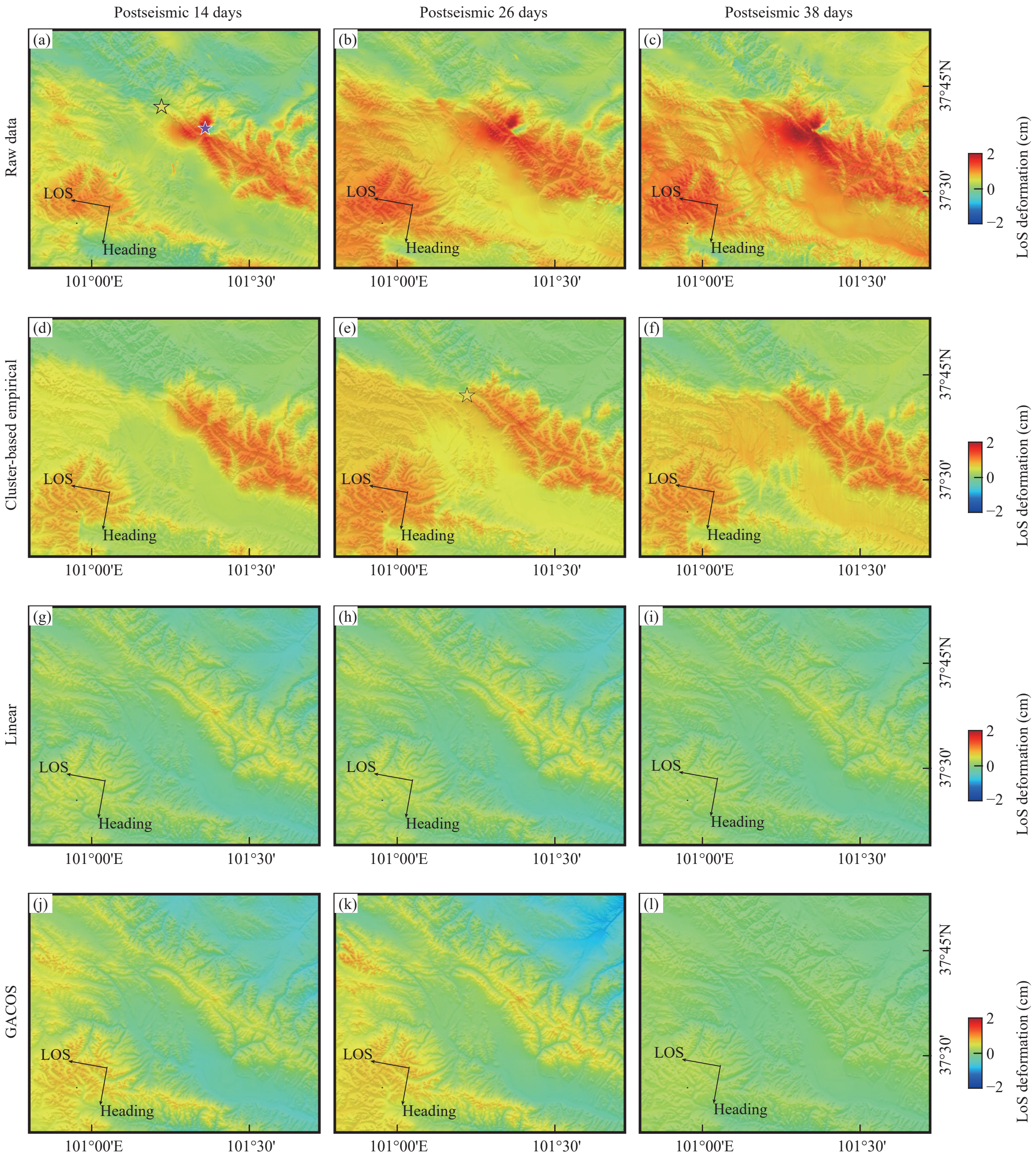

Figure S2. Postseismic LOS displacement from raw interferograms and atmospheric delay correction obtained by different methods. (a–c) represent raw interferograms spanning 2 days after mainshock to 14 days, 26 days and 38 days after mainshock respectively. (d–f) represent the atmospheric delay corrections derived by the K-means clustering method. (g–i) represent atmospheric corrections by linear function, and (j–l) atmospheric corrections derived by GACOS. Note that the dates order is the same for different row.

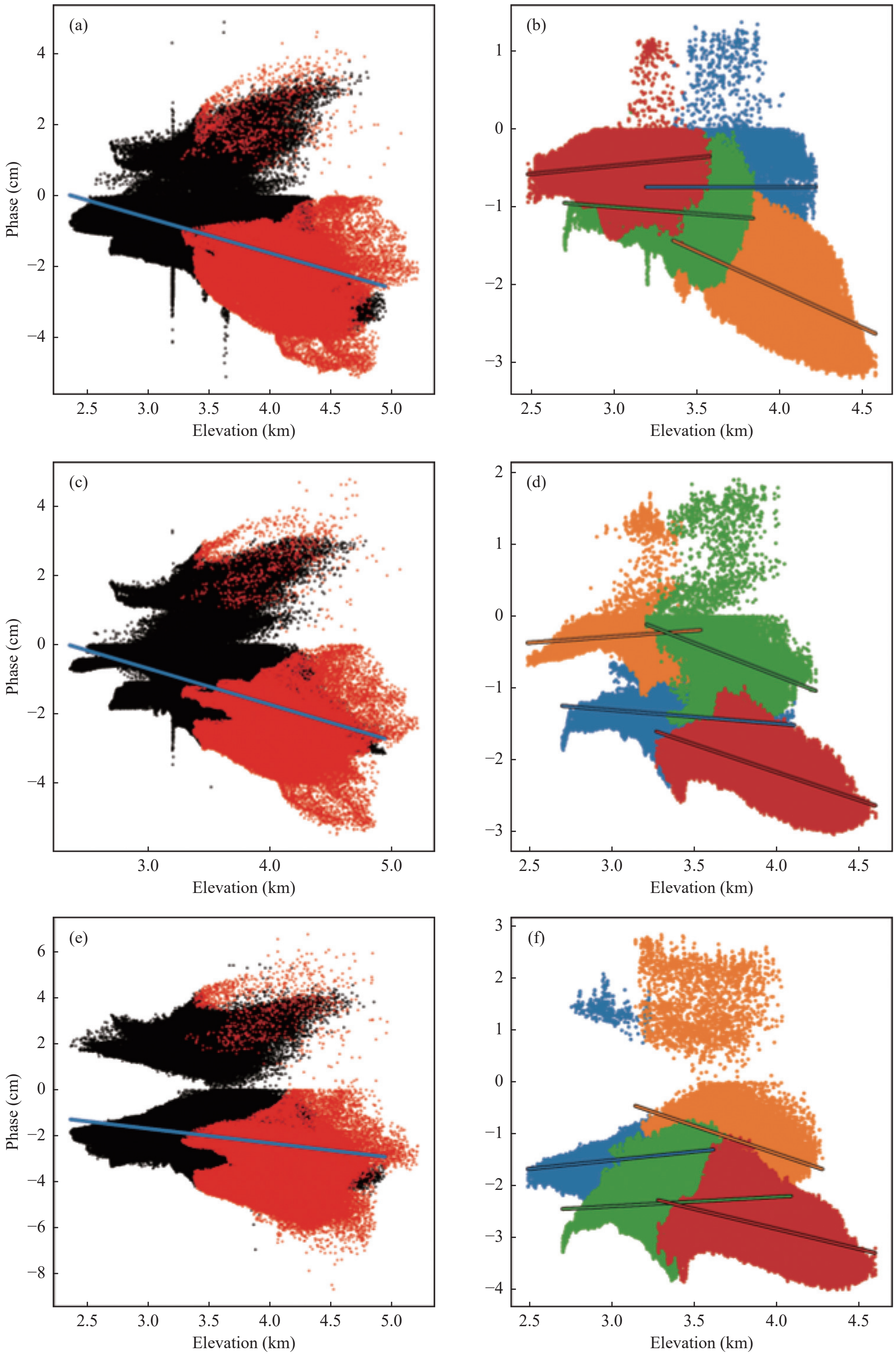

Figure S3. Elevation versus phase plot for postseismic interferograms. (a), (c) and (e) represent the best linear fit results (red points denote the masked deformation data). (b), (d) and (f) represent linear fits separated by four clusters.

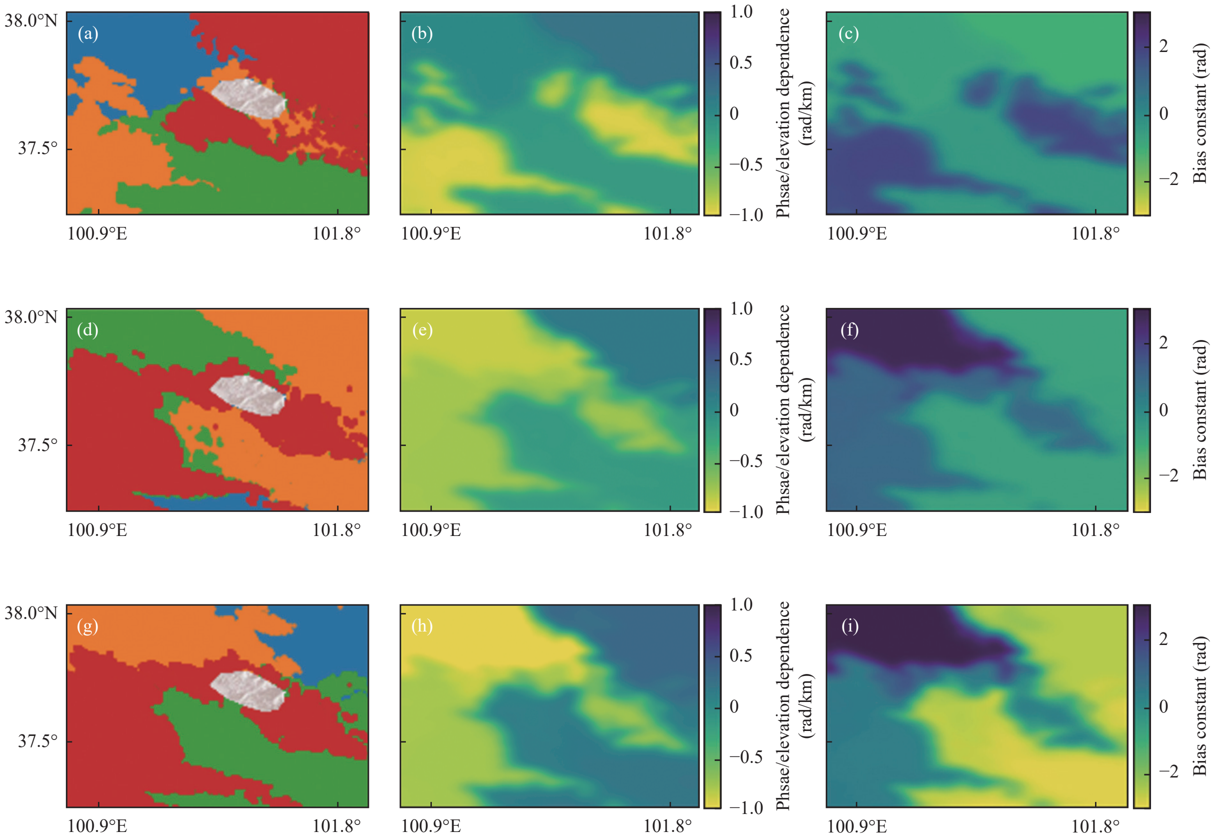

Figure S4. Clustering results and inferred parameters of the cluster-based empirical function method. (a), (d) and (g) represent the four-clusters maps of the postseismic interferograms from Figure S1. (b), (e) and (h) represent the slops of linear function, and (c), (f) and (i) represent the intercepts of linear function.

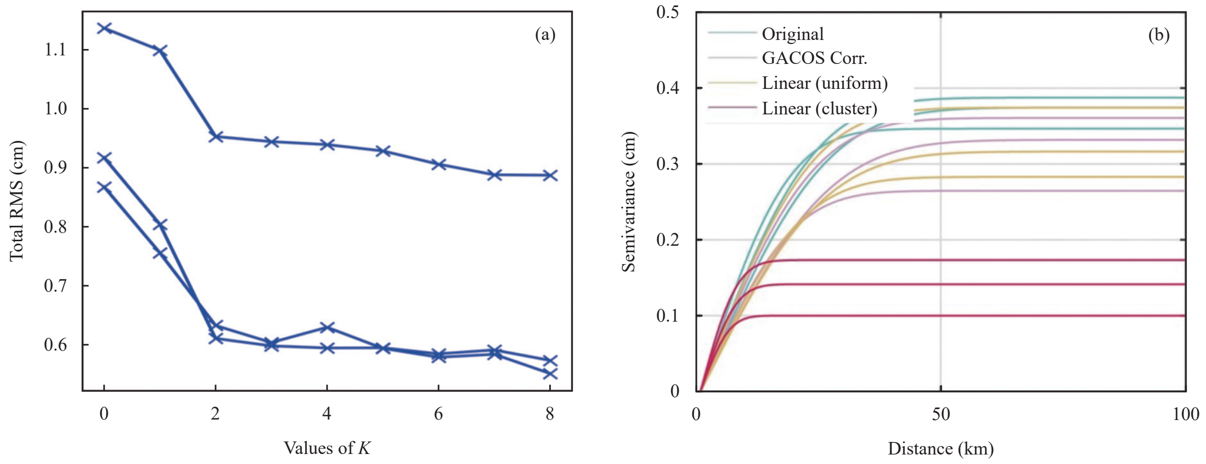

Figure S5. The trade-off curve used to determine the cluster number, alongside a comparison of correction effects from different methods. (a) The RMS of the residuals of the postseismic interferograms versus the number of clusters. Zero clusters indicates no correction was applied, and one cluster indicates the simple linear function was applied. (b) Semivariogram values for the postseismic interferograms with and without atmospheric delay corrections.

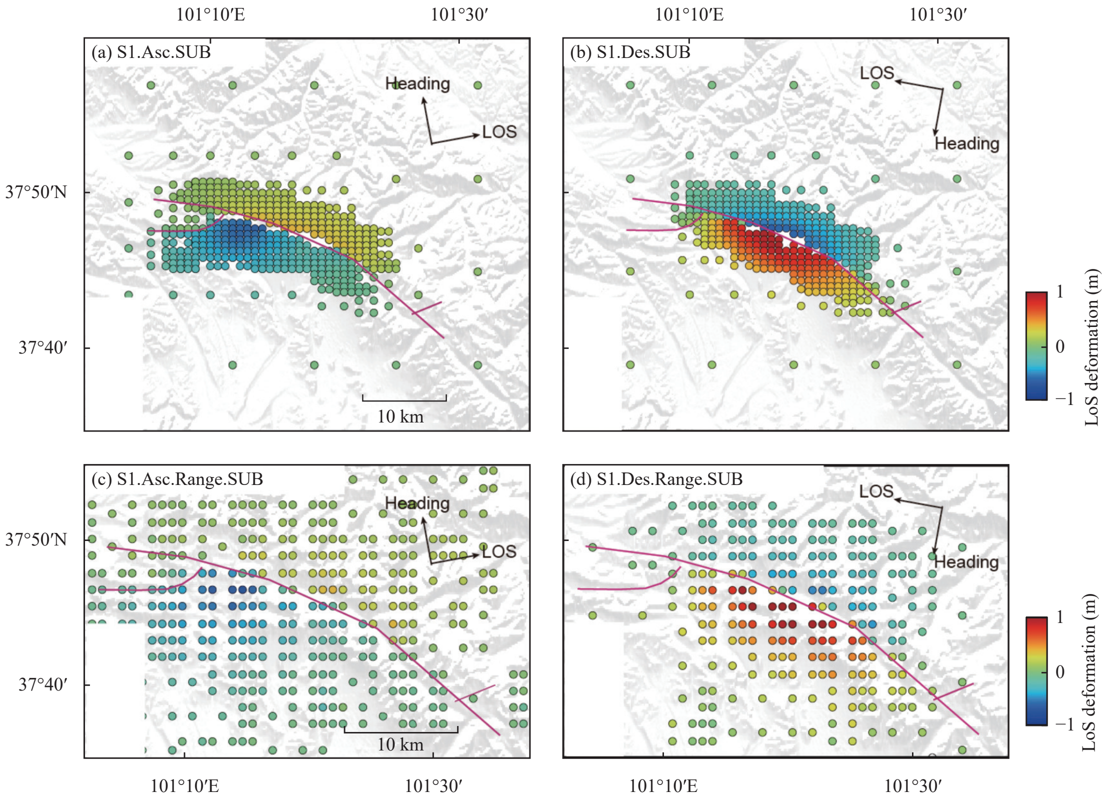

Figure S6. Quadtree subsampled InSAR data for (a) the cumulative ascending coseismic deformation, (b) the descending cumulative coseismic deformation, (c) the cumulative ascending range offset fields and (d) the cumulative descending range offsets field. Cold color values indicate LOS/Range displacement towards the satellite.

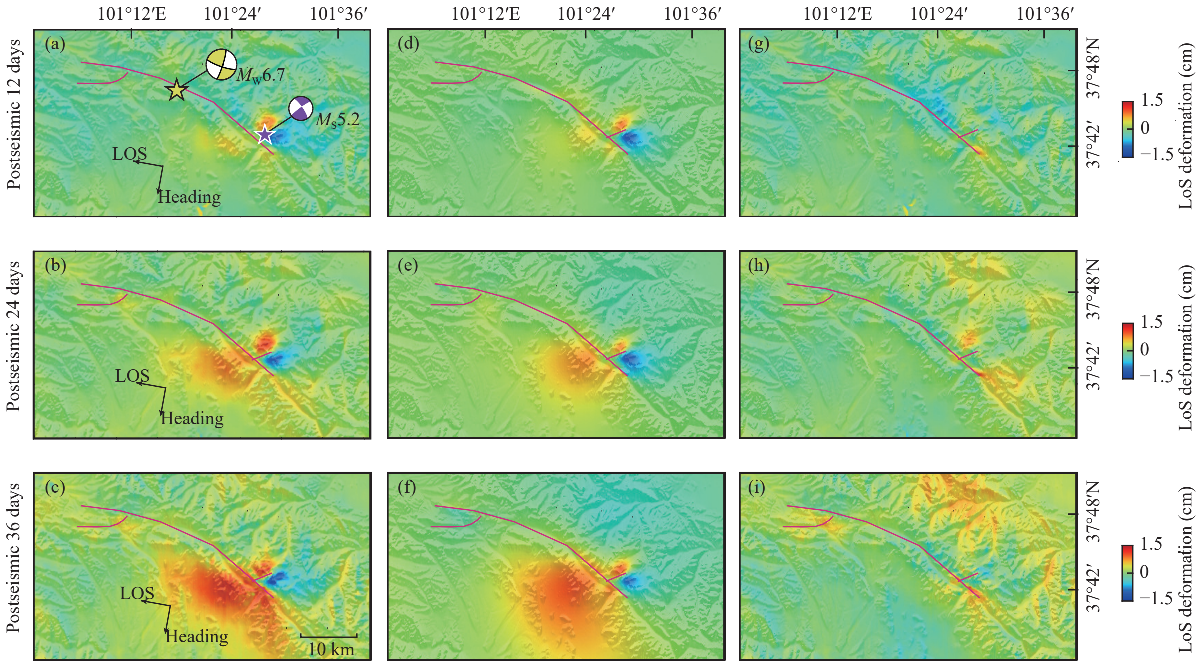

Figure S7. Postseismic deformation field and modeling results of the postseismic afterslip and the second largest aftershock. (a–c) The observed deformation of afterslip and the largest aftershock spanning 14 days, 26 days, and 38 days after the mainshock respectively. (d–f) The modeled deformation. (g–i) The residuals between the observed and modeled deformation. The magenta lines represent the top trace of the modeled fault.

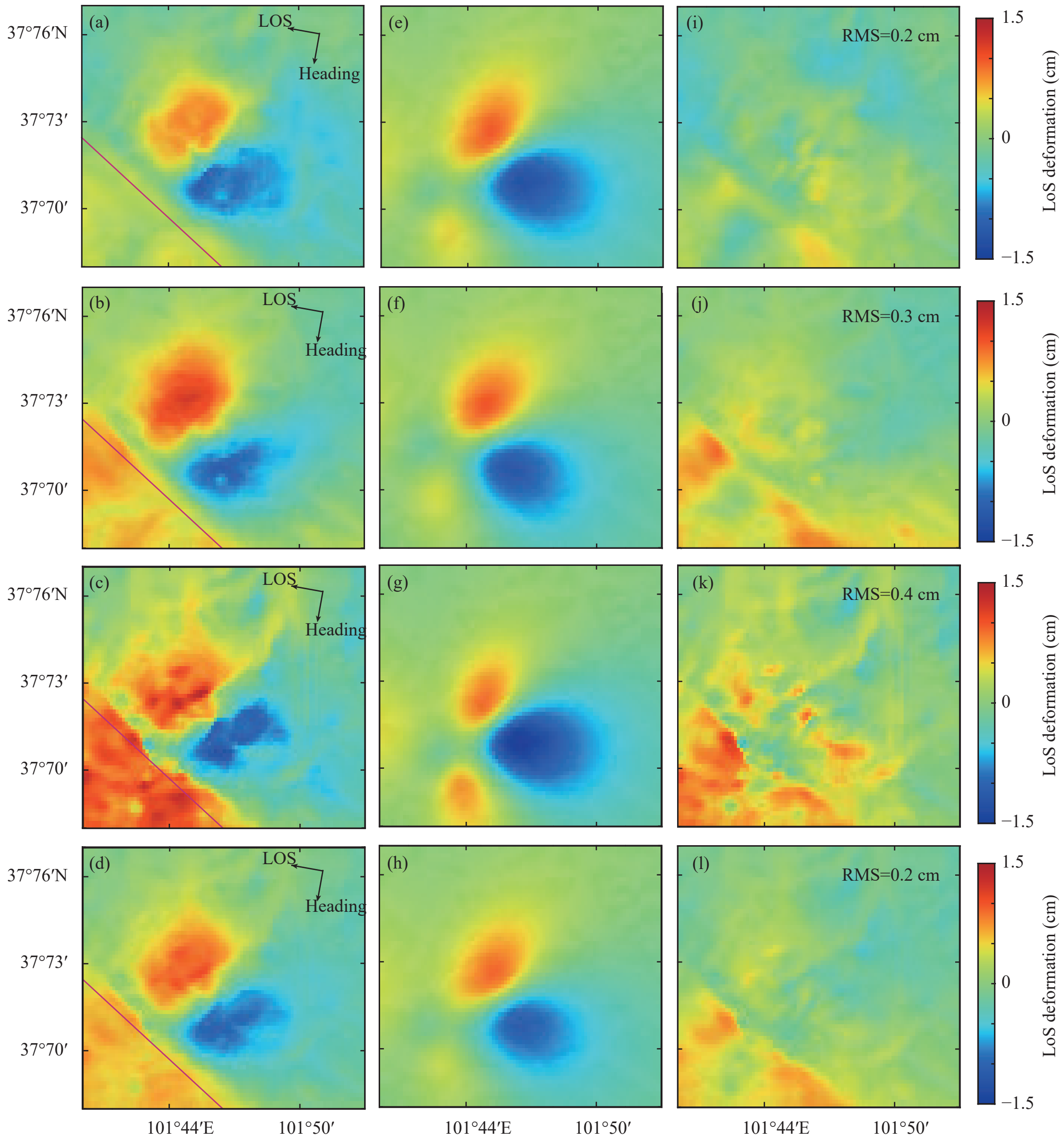

Figure S8. Deformation field and modeling results of the second largest aftershock. (a–c) represent the observed deformation of aftershock corresponding to interferograms spanning 14 days, 26 days, and 38 days after the mainshock respectively. (d) represents the deformation field of the stacking result of all postseismic interferograms. (e–h) are the modeled aftershock coseismic deformation. (i–l) are the residuals between the observed and modeled deformation. The pink line represents the SAR-inferred rupture fault in this study.

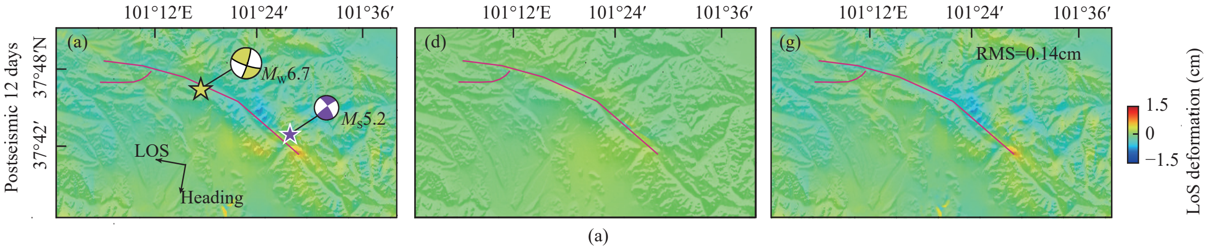

Figure S9. Deformation field and modeling results of the postseismic afterslip. (a–c) The observed deformation of afterslip spanning 14 days, 26 days, and 38 days after the mainshock respectively. (d–f) The modeled deformation. (g–i) The residuals between the observed and modeled deformation.

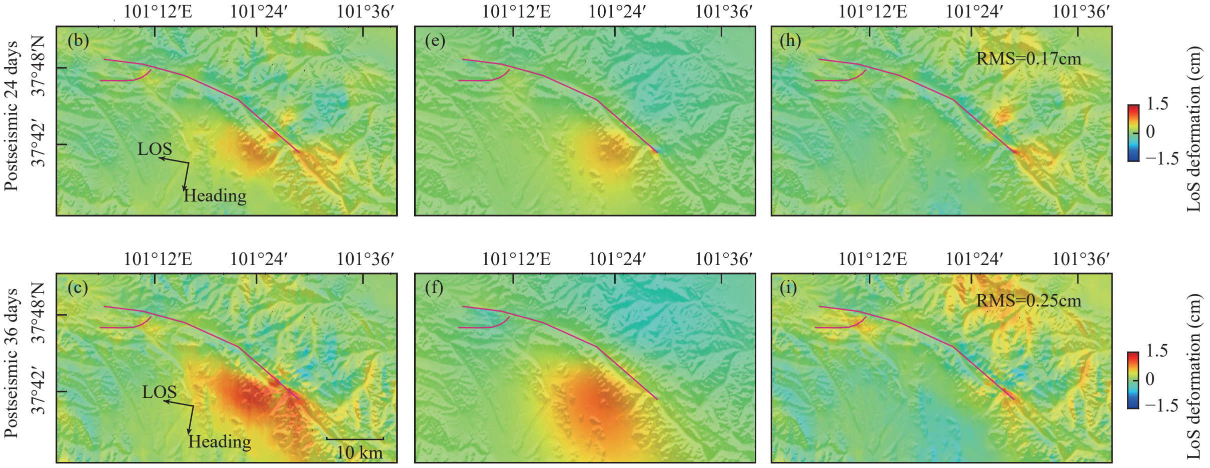

(b)

Figure S9. Continued.

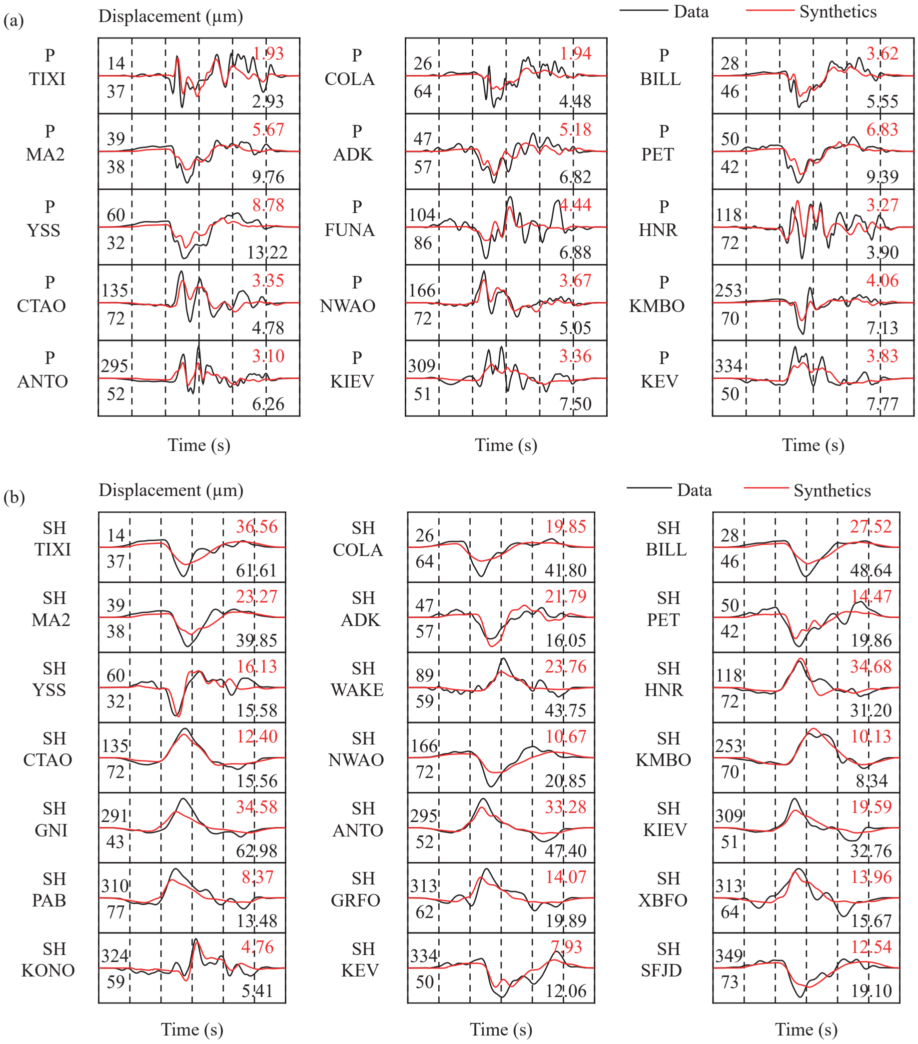

Figure S10. Observed and modeled seismic data. (a) Comparison between the synthetic waveforms and the observed teleseismic P-wave records (displacement). The maximum amplitude of the observed (black font) and synthetic waveform (red font) is shown to the right of each waveform, in micrometers. The azimuth and distance in degrees are shown at the beginning of each record with the azimuth on top. (b) is the same with (a), but for the teleseismic SH-wave records.

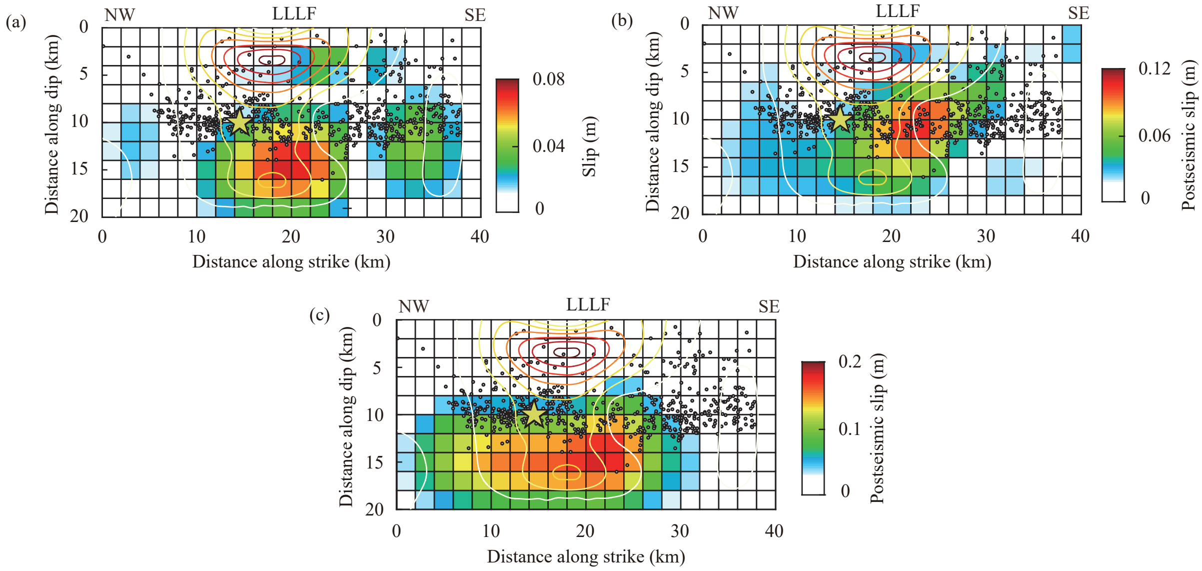

Figure S11. 2-D view of the coseismic slip and afterslip models. (a–c) are afterslip models corresponding to 14 days, 26 days and 38 days after the mainshock, respectively. The yellow star represents the epicenter of mainshock. The gray dots denote the relocated aftershocks. The smoothed contour lines with 0.5 m interval are coseismic slip model. The color table of the coseismic slip is the same for (a–c).

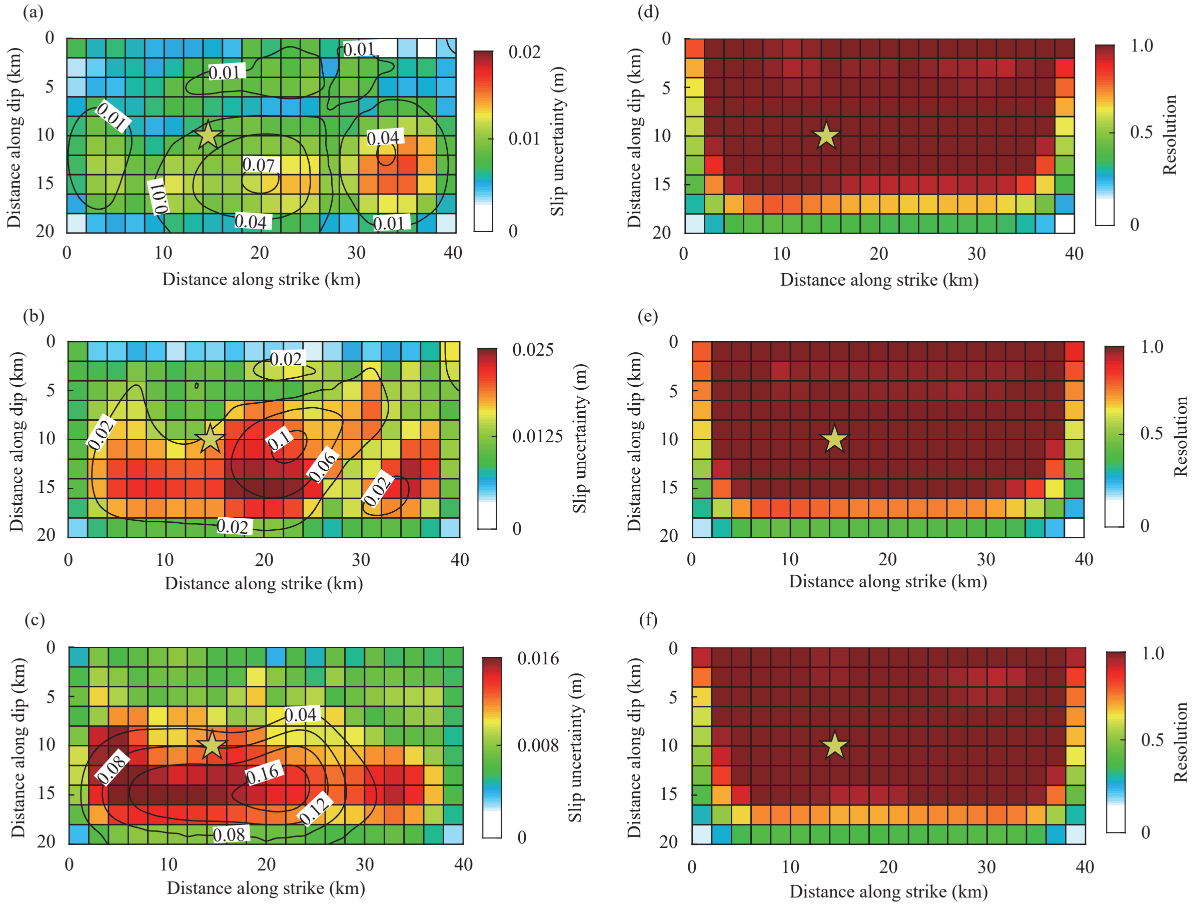

Figure S12. Slip uncertainty and resolution operator for different afterslip models. (a–c) show the slip uncertainties for the afterslip model spanning 14 days, 26 days, and 38 days after mainshock. The contour lines represent the derived afterslip models. (d–f) are the same with (a–c), but for the slip resolution.

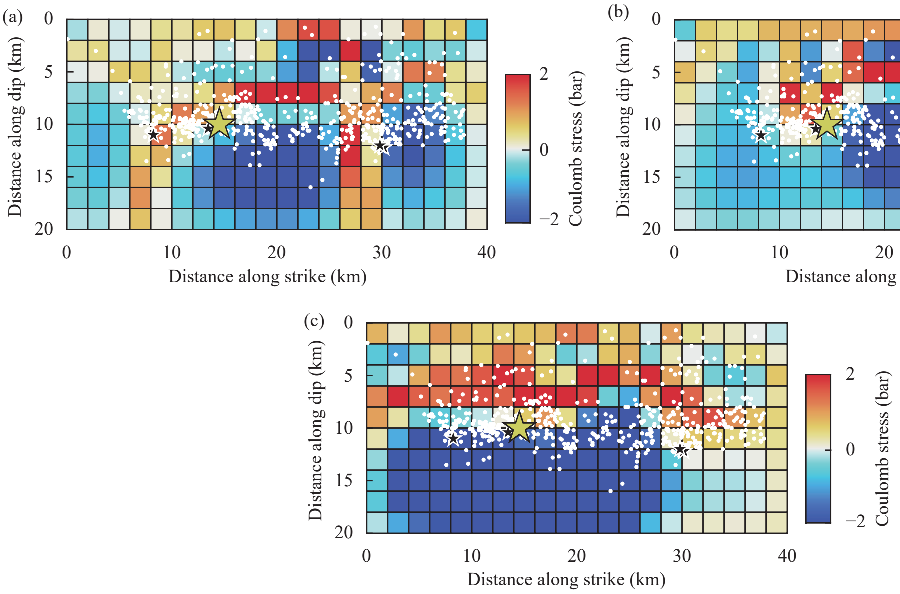

Figure S13. Static Coulomb stress on seismogenic fault surface induced by afterslip corresponding to (a) 14 days, (b) 26 days, and (c) 38 days after mainshock, respectively. The yellow stars represent the epicenter of mainshock. The black stars represent the larger aftershocks (*M*>4.0). Other smaller aftershocks are denoted by white dots.

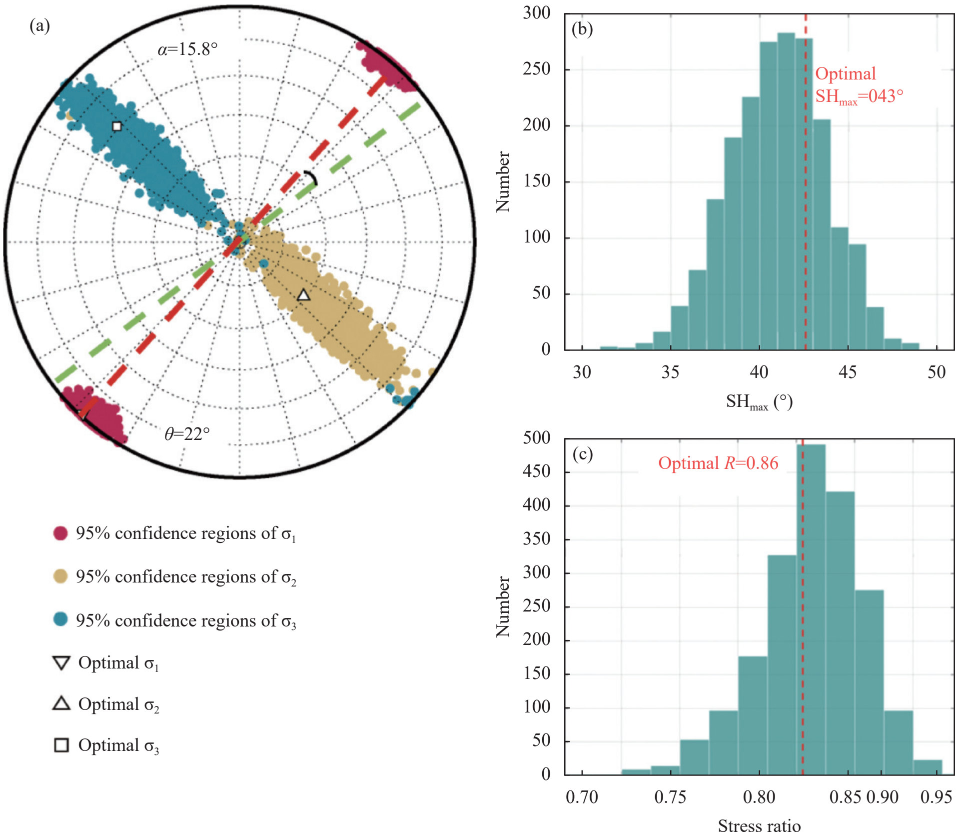

Figure S14. The stress tensor inversion. (a) is the result of stress inversion for epicentral region of the 2022 Menyuan earthquake, the dashed red line and the green line indicate the direction of the maximum principle stress and the strike of conjugated fault hosting the second largest aftershock, respectively. (b) and (c) are the histograms of $\mathrm{SH_{max}}$ and Stress ratio from 2000 bootstrap samples, respectively. Dashed red lines in (b) and (c) are optimal $\mathrm{SH_{max}}$ and stress ratio, respectively.

Table S1. Details of SAR acquisitions for coseismic and postseismic deformation analysis.

Satellite	Track	Mastar a-mo-d	Slave a-mo-d	Perp.B(m)	Direction	Epoch
Sentinel-1A	T128	2022-01-05	2022-01-17	39	Ascending	Coseismic
Sentinel-1A	T33	2021-12-29	2022-01-10	56	Descending	
Sentinel-1A	T33	2022-01-10	2022-01-22	20	Descending	Postseismic
Sentinel-1A	T33	2022-01-10	2022-02-03	−11	Descending	
Sentinel-1A	T33	2022-01-10	2022-02-15	34	Descending	

Note: Per.B is the length of perpendicular baselines; Epoch is the covering period of the interferograms.

Table S2. Data noise sill variance and covariance value and coefficients a, b for exponential model $C(h) = a \cdot \exp\ (-h/b)$.

Data	Covariance (cm^2)	Sill variance a (cm^2)	Range b (km)	Epoch
S1.T33.LOS	0.39	0.63	12.14	Coseismic
S1.T128.LOS	1.04	1.64	19.07	
S1.T33.Range	41.46	65.59	3.56	
S1.T128.Range	31.44	49.74	2.92	
S1.T33.LOS (12 days)	0.013	0.021	7.68	Postseismic
S1.T33.LOS (24 days)	0.007	0.011	5.07	
S1.T33.LOS (36 days)	0.017	0.028	6.195	

Note: Epoch is the covering period of the interferograms.

Table S3. Initially set parameters and optimal mechanism parameters obtained through the nonlinear inversion of the Menyuan mainshock.

	Length (km)	Width (km)	Depth (m)	Dip (°)	Strike (°)	*X* center (m)	*Y* center (m)	Strike slip (m)	Dip slip (m)
Start	30	10	5000	−80	284	0	0	−3	0
Step	1	1	1000	10	15	100	100	0.02	0.02
Lower	10	2	0	−90	260	−100000	−100000	−5	−2
Upper	60	20	20000	−60	300	100000	100000	1	1
Optimal	18.27	7.26	355.6	−78.9	288.9	−1085.3	523.8	−2.4	−0.3

Note: The fault is in a left-handed coordinate system, and the reference point of the local coordinate is at (101.3°E, 37.78°N) in terms of longitude and latitude.

Table S4. Initially set parameters and optimal mechanism parameters obtained through the nonlinear inversion of the second largest aftershock.

	Length (km)	Width (km)	Depth (m)	Dip (°)	Strike (°)	*X* center (m)	*Y* center (m)	Strike slip (m)	Dip slip (m)
Start	1.5	1.5	750	−87	65	16200	−6397	0	0
Step	0.1	0.1	100	10	2	100	100	0.1	0
Lower	1	0.5	100	−89.9	62	12000	−8000.5	−1.5	0
Upper	10	10	5000	−76	68	18000	−3500.2	3.0	0
Optimal	3.2	3.1	992	−82.6	62	14085.4	−7611.4	0.16	0

Note: The fault is in a left-handed coordinate system, and the reference point of the local coordinate is at (101.3°E, 37.78°N) in terms of longitude and latitude.

Table S5. Stress tensor parameters as obtained from focal mechanisms in the epicenter region.

N	σ_1(°) az./pl.	σ_2(°) az./pl.	σ_3(°) az./pl.	R	α(°)	Stress regime	SH_{max}
24	222/1.3	130/61	313/29	0.86	15.8	SS	043

Note: N is the number of focal mechanisms; σ_1, σ_2, and σ_3 are the azimuth and plunge angles; stress ratio $R=(\sigma_1-\sigma_2)/(\sigma_1-\sigma_3)$, $0\leq R\leq 1$; α is the misfit angle; SH_{max} is the maximum horizontal compressive stress orientation.

Table S6. Fault plane solutions for earthquakes in the 2022 Menyuan epicentral region. Except for the last focal mechanism determined by our geodetic inversion results in this table, the other focal mechanisms are collected from the National Earthquake Data Center (https://data.earthquake.cn, 2022. DOI: 10.12080/nedc.11.ds.2022.0004).

a-mo-d	h:min	Lat(°N)	Lon(°E)	Depth(km)	MgType	Mg	Strike1(°)	Dip1(°)	Rake1(°)	Strike2(°)	Dip2(°)	Rake2(°)
2009-09-30	42:17.0	37.529	102.226	5	M_L	3.5	200	87	175	290	85	3
2009-12-7	32:23.7	37.712	102.272	7	M_L	3.5	133	51	129	261	53	52
2009-12-19	25:57.5	38.494	101.539	7	M_L	4.5	313	15	113	109	76	84
2010-05-31	32:21.8	37.505	102.267	8	M_L	3.6	346	89	−167	256	77	−1
2010-10-11	55:01.7	37.508	102.241	6	M_L	3.9	353	77	−176	262	86	−13
2010-12-13	19:30.4	38.332	100.952	6	M_L	4.1	305	51	71	154	43	112
2011-02-22	38:33.3	37.624	102.255	8	M_L	4.1	72	57	43	315	55	138
2012-05-11	18:09.1	37.75	102	16	M_S	4.9	267	80	16	174	74	170
2013-06-21	50:55.7	37.541	102.238	6	M_L	3.8	243	69	−17	339	74	−158
2013-09-20	37:01.4	37.73	101.53	15	M_S	5.3	360	68	120	123	37	39
2014-02-22	56:16.0	37.61	102.27	6	M_S	4.5	161	85	178	251	88	5
2014-03-12	30:49.1	37.622	102.259	7	M_L	4.1	198	71	−180	108	90	−19
2015-03-30	59:15.0	38.563	101.509	8	M_L	3.5	172	58	−169	76	81	−32
2015-11-23	02:41.4	38.01	100.39	10	M_S	5.3	109	57	15	11	77	146
2016-01-21	13:12.0	37.66	101.65	10	M_S	6.4	153	44	96	325	46	84
2016-01-21	18:24.0	37.668	101.609	10	M_L	4.1	95	54	−6	189	85	−144
2016-01-23	02:50.7	37.688	101.6	6	M_L	3.6	317	76	166	50	76	14
2016-07-10	35:51.4	37.627	101.613	12	M_L	3.7	330	40	142	91	67	57
2016-08-13	29:48.0	37.69	101.56	9	M_S	4.7	97	57	33	348	63	142
2016-11-14	39:44.2	37.821	102.259	8	M_L	4.4	174	60	137	289	54	38
2017-07-12	42:17.0	37.692	101.591	9	M_L	4.3	315	39	121	97	57	67
2018-08-26	29:41.2	37.698	102.24	6	M_L	4.2	129	73	87	319	17	100
2019-09-16	48:39.0	38.57	100.31	10	M_S	5	146	49	112	294	46	67
2022-01-08	01:45.5	37.77	101.27	12.9	M_W	6.76	108.9	78.9	7.3	–	–	–